In Silico Elucidation of Key Drivers of *Staphyloccocus aureus*–*Staphyloccocus epidermidis*–Induced Skin Damage in Atopic Dermatitis Lesions

Jamie Lee[1,3], Ahmad A. Mannan[1,3], Takuya Miyano[1], Alan D. Irvine[2] and Reiko J. Tanaka[1]

Staphylococcus aureus (SA) colonizes and can damage skin in atopic dermatitis lesions, despite being commonly found with *Staphylococcus epidermidis* (SE), a commensal that can inhibit SA's virulence and kill SA. In this study, we developed an *in silico* model, termed a virtual skin site, describing the dynamic interplay between SA, SE, and the skin barrier in atopic dermatitis lesions to investigate the mechanisms driving skin damage by SA and SE. We generated 10^6 virtual skin sites by varying model parameters to represent different skin physiologies and bacterial properties. *In silico* analysis revealed that virtual skin sites with no skin damage in the model were characterized by parameters representing stronger SA and SE growth attenuation than those with skin damage. This inspired an *in silico* treatment strategy combining SA-killing with an enhanced SA–SE growth attenuation, which was found through simulations to recover many more damaged virtual skin sites to a non-damaged state, compared with SA-killing alone. This study demonstrates that *in silico* modelling can help elucidate the key factors driving skin damage caused by SA–SE colonization in atopic dermatitis lesions and help propose strategies to control it, which we envision will contribute to the design of promising treatments for clinical studies.

Keywords: Atopic dermatitis, Mathematical modelling, Microbial interactions, Skin damage

JID Innovations (2024);**4:**100269 doi:10.1016/j.xjidi.2024.100269

INTRODUCTION

Atopic dermatitis (AD) is a debilitating disease of dry, itchy, and inflamed skin. It affects around 20% of children and 3% of adults worldwide (Langan et al, 2020; Nutten, 2015), with incidences on the increase (Asher et al, 2006). Patients with AD typically have an impaired skin barrier function, such as genetic defects in FLG (Palmer et al, 2006) and higher pH (Geoghegan et al, 2018). An impaired skin function can lead to dysbiosis of the skin microbiome (Bjerre et al, 2021), where bacterial diversity is severely reduced and contains high fractions of *Staphylococcus aureus* (SA) (Byrd et al, 2017; Kong et al, 2012). SA can proliferate to such high populations in AD lesions that they switch to a skin damaging phenotype (Hwang et al, 2021) through quorum sensing (QS) activation of its accessory gene regulator (agr) system (Jenul and Horswill, 2019; Nakamura et al, 2013) and expression of virulence factors phenol soluble modulin (PSM) α and PSM δ (Nakagawa et al, 2017; Nakamura et al, 2013; Nakatsuji et al, 2016; Williams et al, 2019, 2017). Skin damage can also induce the loss of the acid mantle (Elias, 2017), further increasing SA growth (Iyer et al, 2021; Miajlovic et al, 2010).

The most prevalent coresident with SA in AD skin lesions is coagulase negative staphylococci (CoNS), *Staphylococcus epidermidis* (SE) (Kong et al, 2012). Considered a sentinel of healthy skin (Fournière et al, 2020), SE fortifies the skin barrier integrity with ceramides (Zheng et al, 2022) and can also actively defend against SA invasion by secreting products from its activated QS agr system. These QS products include autoinducing peptides (AIPs) that inhibit the expression of SA virulence (Otto et al, 2001; Williams et al, 2019) and of PSMs, such as PSM γ and PSM δ, which can kill SA (Cogen et al, 2010; Hardy et al, 2020). SE and SA are expected to interact through products of their QS agr system in AD lesions because SE's agr system is reported to be active *in vivo* (Teichmann et al, 2022; Zhou et al, 2020). However, the outcome of their interactions remains unclear.

To investigate the outcome of the SA–SE interactions and their effect on the skin, in this study, we built an *in silico* model of the dynamic interactions between SA, SE, and the skin barrier, using a bottom-up approach (Tanaka and Ono, 2013). The model considers QS-induced damage by both SA and SE because skin damaging by SA is well-established (Williams et al, 2019), and some SE isolates have also been

[1]*Department of Bioengineering, Imperial College London, London, United Kingdom; and* [2]*Clinical Medicine, Trinity College Dublin, The University of Dublin, Dublin, Ireland*

[3]*These authors contributed equally to this work.*

Correspondence: Reiko J. Tanaka, Department of Bioengineering, Imperial College London, South Kensington Campus, London SW7 2AZ, United Kingdom. E-mail: r.tanaka@imperial.ac.uk

Abbreviations: AD, atopic dermatitis; agr, accessory gene regulator; AIP, autoinducing peptide; CoNS, coagulase negative staphylococci; PSM, phenol soluble modulin; QS, quorum sensing; SA, *Staphylococcus aureus;* SE, *Staphylococcus epidermidis*

Received 7 June 2023; revised 22 January 2024; accepted 29 January 2024; accepted manuscript published online XXX; corrected proof published online XXX

Cite this article as: JID Innovations 2024;4:100269

discovered to damage the skin in AD through its agr QS—activated expression of extracellular cysteine protease EcpA (Cau et al, 2021).

We built the model on the basis of a previously published model of AD pathogenesis (Miyano et al, 2022) where Miyano et al (2022) considered the interaction between SA and a generic non-damaging CoNS. Their model simulations suggested that AD treatment by antibiotics may fail to recover skin barrier integrity (Miyano et al, 2022) because antibiotics are usually unspecific to SA and may disproportionately kill off other CoNS, reducing their ability to inhibit SA virulence and prevent skin damage. They predicted that the targeted killing of SA only (SA-killing) should enable skin barrier recovery. However, the efficacy of SA-killing is unclear if CoNS in admixture with SA at the skin site, such as SE, is also skin damaging. Furthermore, the long-term efficacy of SA-killing could not be investigated by Miyano et al (2022)'s model because some of the clinical data used to develop the model only evaluated the efficacy of treatment over a short duration (eg, 10 days). The systems behavior may still change dynamically beyond this time point.

In this study, we generate 10^6 virtual skin sites describing AD lesions with SA and SE colonization by varying the parameters representing a wide range of skin physiologies and SA and SE strains in our *in silico* model. We simulate the steady states of each virtual skin site and analyze whether the virtual skin site converges to a damaged skin state, that is, a state in our model that represents skin damage by SA and/or SE. We then evaluate the impact of applying a treatment to virtual skin sites in a damaged skin state. *In silico* simulations demonstrate that a SA-killing treatment mostly fails to recover damaged skin states to a non-damaged skin state in the model. Assessment of model parameters characterizing different virtual skin sites reveals key interactions that drive the emergence of a damaged skin state in the model, suggesting an alternative *in silico* treatment strategy combining SA-killing with an enhanced attenuation of SA and SE growth. Simulations of this alternative *in silico* treatment strategy to all virtual skin sites in a damaged skin state predict that more of these virtual skin sites can recover to a non-damaged skin state in the model. This work demonstrates that *in silico* modeling can be an effective tool to elucidate system outcomes and can help to rationally guide the implementation of successful treatment strategies applicable to a wide range of patients in the clinic.

RESULTS

In silico model of AD lesions with SA—SE colonization

We developed an *in silico* model that captures our current knowledge of the systems-level dynamic interactions between SA, SE, and the skin barrier in AD lesions (Figure 1, model formulation detailed in Supplementary Materials and Methods). The model is a system of 3 ordinary differential equations describing the growth dynamics of SA and SE, how they are affected by the skin barrier, their population density—dependent expression of QS-agr products, the resulting interactions between the 2 bacteria, and their damaging of the skin barrier. The dynamics are defined by 17 parameters (Supplementary Table S1), with the nominal value of 9 parameters derived from previously published studies and the values of the remaining 8 parameters chosen on the basis of knowledge of the field (Supplementary Materials and Methods).

The key interactions included in our model were identified on the basis of empirical evidence from previously published *in vivo* (Cau et al, 2021; Hoffman et al, 2014; Koster, 2009; Williams et al, 2019) and *in vitro* (Iyer et al, 2021; James et al, 2013; Miajlovic et al, 2010; Nakatsuji et al, 2017; Olson et al, 2014; Toribio et al, 2018; Williams et al, 2019) studies. As SA and SE populations grow, they secrete AIPs, which trigger the activation of the QS-switch once AIPs reach a threshold concentration. The activation of the QS-switch in turn activates the expression of antimicrobial peptides that can kill the other species (Cogen et al, 2010; Nakatsuji et al, 2017), virulence factors that can damage the skin (Cau et al, 2021; Williams et al, 2019), and AIPs that can interfere with the other species' QS sensing module (Otto et al, 2001; Williams et al, 2019). For simplicity, we assumed that the threshold concentration of AIPs that activate the QS-switch is

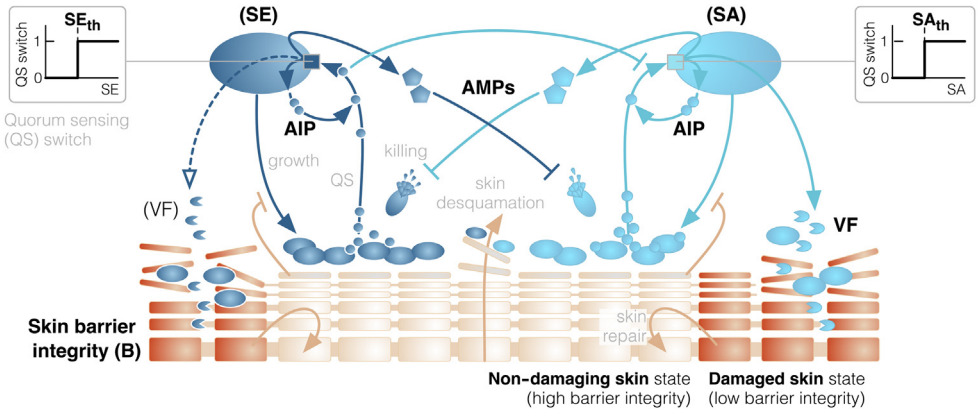

Figure 1. Schematic of the *in silico* model of AD lesions with SA—SE colonization. The model describes interactions between SA (light blue ovals), SE (dark blue ovals), and barrier integrity (B, rectangles) by a system of ordinary differential equations. The agr QS system in both bacteria is assumed to be activated in a switch-like manner at threshold population densities SA_{th} and SE_{th} (inset plots) to synthesize several products, namely AIPs (dots), AMPs (pentagons) that kill the other species, and virulence factors (sector shape) that damage the skin barrier. SE AIPs inhibit SA QS activation but not vice versa. VF denotes virulence factor. AD, atopic dermatitis; agr, accessory gene regulator; AIP, autoinducing peptide; AMP, antimicrobial peptide; QS, quorum sensing; SA, *Staphylococcus aureus*; SE, *Staphylococcus epidermidis*.

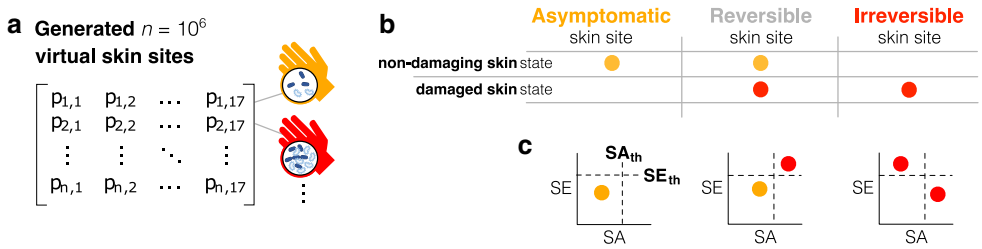

Figure 2. Three types of virtual skin sites. (**a**) Illustration of 10^6 virtual skin sites generated. (**b**) Three types of virtual skin sites were defined by whether the stable skin state converged to non-damaged (yellow) or damaged (red). (**c**) Representative example plots of the stable steady state SA and SE populations and barrier integrity (dot color) for each type of skin site. Dashed lines represent thresholds of SA (SA_{th}) and SE (SE_{th}) populations that activate their QS-switch, which we varied in our analysis. QS, quorum sensing; SA, *Staphylococcus aureus*; SE, *Staphylococcus epidermidis*.

directly proportional to a threshold population density, denoted as SA_{th} and SE_{th} (Figure 1, inset). The skin barrier was assumed to continuously repair and desquamate while attenuating the growths of SA and SE. We defined the modelled skin barrier to be in a damaged or non-damaged state, depending on whether the skin is being damaged by SA and/or SE or neither, as reflected in the barrier integrity value being low ($0<B<1$) or high ($B=1$) in the model, respectively.

Three qualitatively distinct virtual skin sites

We first investigated the long-term outcomes of SA−SE−skin barrier interactions, also known as the stable steady states of the system. To explore how different model parameter values may lead to different steady states, we generated 10^6 virtual skin sites (Figure 2a) by randomly selecting 10^6 sets of 17 model parameter values, each of which was sampled from a range defined in Supplementary Table S1. Variations in the parameter values represent varying skin physiologies and functional differences in SA and SE strains between AD lesions. For each virtual skin site, we numerically determined all the stable steady states that the system eventually converged onto (Materials and Methods and Supplementary Materials and Methods provide the details). We define a state to be stable if the system converges back to it after a small perturbation is added to the populations of SA or SE or skin barrier integrity value.

We discovered 3 qualitatively distinct virtual skin sites (Figure 2b). Specifically, we define a virtual skin site as (i) asymptomatic if it converges to a single non-damaged skin state (Figure 2b, left), (ii) reversible if it converges to both non-damaged and damaged skin states (Figure 2b, middle), and (iii) irreversible if it converges only to damaged skin states (Figure 2b, right). We use the terms reversible and irreversible to distinguish between sites that have a non-damaged skin state that the system could be reversed back to, given the right perturbation such as an *in silico* treatment, versus sites that have no non-damaged skin states. The population densities of SA and SE for all virtual skin sites are shown in Supplementary Figure S1, with examples of each qualitatively distinct skin site illustrated in Figure 2c.

Simulated temporary SA-killing treatment often fails to recover a non-damaged state in the model

We then investigated whether a temporary SA-killing, as proposed by Miyano et al (2022), could bring a damaged virtual skin site back to a non-damaged skin state. To simulate the temporary SA-killing treatment, we applied a fixed strength of SA-killing (model parameter δ_{AS}) for a fixed duration to all damaged virtual skin sites (791,168 reversible and irreversible virtual skin sites of the 10^6 sites) (Figures 3a). We measured the success rate of the given *in silico* SA-killing treatment by the proportion of all treated virtual skin sites that moved out of the damaged skin state and converged to a stable non-damaged skin state. We also explored how changing the strength and duration of the *in silico* treatment affected the success rate.

Simulations of the SA-killing treatment predicted a low success rate (Figure 3b). For example, only 20% of all damaged virtual skin sites recovered to a non-damaged skin state by an *in silico* SA-killing of strength of 3 $days^{-1}$ applied for 2 days. Increasing the simulated treatment strength and duration to 10 $days^{-1}$ and 50 days only increased the success rate to 39% (Supplementary Figure S2). The low success rate was attributed to the large proportion of irreversible virtual skin sites, which did not have a non-damaged skin state to converge to once the *in silico* treatment was removed (Figure 3c).

Simulations of the SA-killing treatment applied to reversible virtual skin sites allowed many of them to recover to a non-damaged skin state in the model (Figure 3d). However, this outcome may depend on the strength and duration of the simulated treatment and whether the virtual skin site has a parameter representing skin-damaging SE. For example, in a particular virtual skin site, the simulated SA-killing with strength of 5 $days^{-1}$ and duration of 4 days led to a see-saw effect where SA was eradicated, but SE overgrew and continued damaging the skin. In contrast, a slightly weaker treatment strength of 4 $days^{-1}$ for the same duration did recover the virtual skin site to a non-damaged skin state (Supplementary Figure S3). This suggests that a specific treatment regime may be required for each virtual skin site to recover to a non-damaged state, making treatment administration impractical in clinical settings. To identify a more promising treatment strategy, we need to understand the key interactions in the model driving a damaged skin state.

Identifying key interactions driving virtual skin sites to a damaged skin state

To unveil the key interactions in virtual skin sites that enable the existence of damaged skin states, we compared the distribution of values of each model parameter for all virtual skin sites with no damaged skin states (ie, asymptomatic sites) against those for all virtual skin sites with a damaged skin state (ie, reversible and irreversible sites) (Supplementary Figure S4). The distribution of values of 6 model parameters

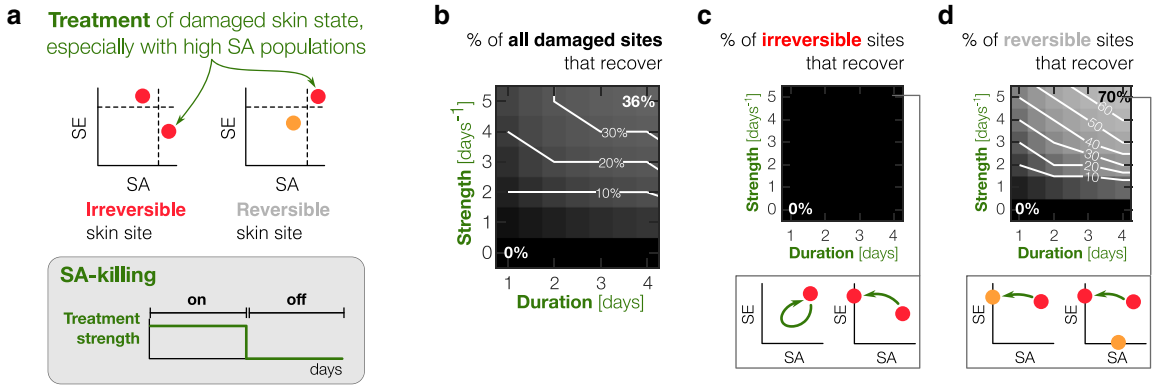

Figure 3. SA-killing treatment mostly fails to recover a non-damaged skin state. (**a**) Illustration of SA-killing treatment applied to damaged states (red dots). (**b**–**d**) Heatmap of successful recovery to a non-damaged skin state in the model for SA-killing treatments of varying strength and duration, as percentage of all (**b**) damaged skin sites, (**c**) irreversible sites, or (**d**) reversible sites. (**c**) Irreversible systems can only converge to damaged states (inset), (**d**) but SA-killing of reversible systems may succeed or fail (inset). SA, *Staphylococcus aureus*.

appeared visually different (Figure 4a): asymptomatic virtual skin sites were characterized by parameters representing faster skin desquamation and recovery, stronger SA and SE growth attenuation, and weaker SA and SE skin damage than reversible and irreversible virtual skin sites (Figure 4b, left).

In addition, we explored the key interactions that drove the difference between irreversible and reversible virtual skin sites. Irreversible virtual skin sites were characterized by parameters representing a weaker attenuation of SA growth by the skin and slower skin desquamation than reversible ones (Figure 4b, right). Further analysis revealed that irreversible virtual skin sites were more specifically characterized by parameters representing a weaker attenuation of the skin damaging species, allowing those species to switch to a skin damaging phenotype. For example, irreversible virtual skin sites with a non-skin-damaging SE had parameters describing a strong attenuation of SE growth (Supplementary Figure S5a), whereas other irreversible virtual skin sites with a skin-damaging SE had parameters describing a weak attenuation of SE growth (Supplementary Figure S5b).

Augmenting SA-killing with stronger SA and SE growth attenuation increases the number of virtual skin sites that recover to a non-damaged skin state

These results suggest that the most effective strategy to recover a non-damaged skin state in the model is by shifting the model parameters to achieve stronger SA and SE growth attenuation, weaker SA and SE skin damage, and faster skin desquamation and recovery (Figure 4b). However, it is difficult to induce a faster skin desquamation and repair in a clinical setting, whereas numerous clinical strategies already exist to attenuate bacterial growth (Khadka et al, 2021; Lee et al, 2016; Nakatsuji et al, 2021), which would consequently weaken SA and SE skin damaging. We thus perceived SA-killing and enhancing SA and SE growth attenuation to be the most translatable treatment to clinical settings.

We therefore propose a dual-action treatment, with a stronger attenuation of SA and SE growth together with temporary SA-killing (Figure 5a; see Materials and Methods) to enable more damaged virtual skin sites to recover to a non-damaged skin state. To implement the dual-action treatment, we simulate the temporary SA-killing and increased the parameters representing the skin's attenuation of SA and SE growths (γ_{AB} and γ_{EB}) by multiplying them with scaling factors γ_{AS} and γ_{ES} (see Materials and Methods). We varied γ_{AS} and γ_{ES} between 1 and 30 to cover a wide range of attenuation strengths.

The simulated dual-action treatment allowed far more damaged virtual skin sites to recover to a non-damaged skin state (Figure 5b) than simulated SA-killing alone (Figure 3b). For example, the *in silico* application of a 20-fold growth attenuation of SA and SE combined with a weak (3 day^{-1}) and short (2 days) SA-killing increased the treatment success

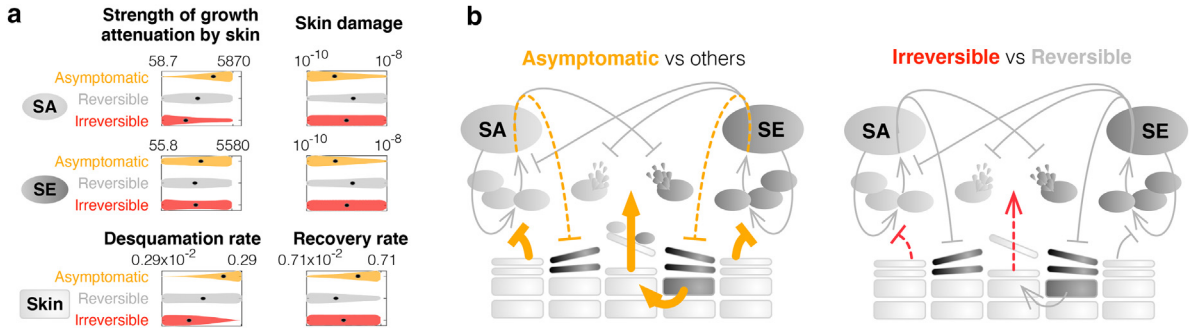

Figure 4. Key model parameters driving a non-damaged and damaged skin state in the model. (**a**) Violin plots of the distributions of values for 6 key parameters that characterize each skin type (black dots represent median values). (**b**) Schematics highlighting stronger, weaker, and no change (bold, dashed, and gray lines, respectively) in interaction strengths that characterize asymptomatic sites (left) and irreversible sites (right).

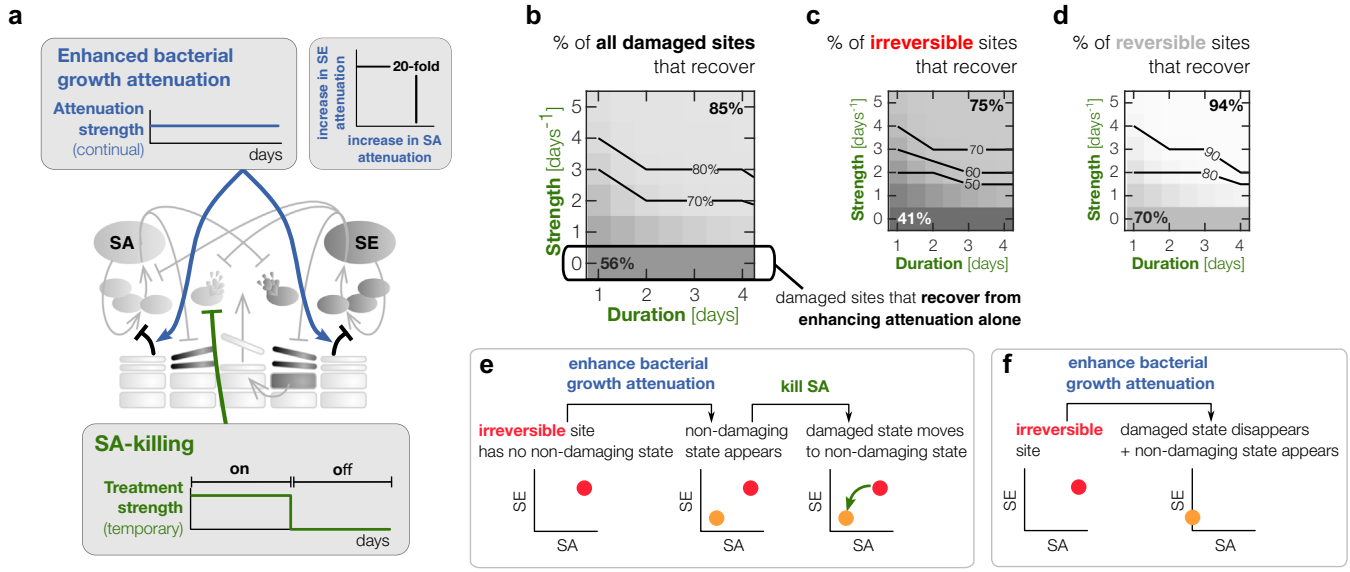

Figure 5. Enhancing SA and SE growth attenuation drastically improves success of SA-killing treatment. (**a**) Illustration of the proposed dual-action treatment. (**b**–**d**) Heatmap of successful recovery to a non-damaged skin state in the model for varying SA-killing and 20-fold enhanced attenuation of SA and SE growth, as percentage of all (**b**) damaged skin sites, (**c**) irreversible sites, or (**d**) reversible sites. (**e, f**) Illustration of how enhancing SA and SE growth attenuation enables irreversible sites to recover (**e**) by allowing the emergence of a non-damaging skin state, which SA-killing can move the damaged state to, or (**f**) by allowing damaged skin states to disappear altogether. SA, *Staphylococcus aureus*; SE, *Staphylococcus epidermidis*.

rate from 20 to 80% (Figures 5b and 3b), although the success rate plateaus for increasing strengths of the growth attenuation of SA and SE (Supplementary Figure S6a).

Why does enhancing the attenuation of SA and SE growth enable more damaged virtual skin sites to recover in the model? *In silico* model analysis suggests that a strong and sustained enhancement of SA and SE growth attenuation resulted in the emergence of a non-damaged skin state for many irreversible virtual skin sites, which SA-killing could move the system to (Figure 5e and Supplementary Figure S6b–d). As a result, a 20-fold enhanced attenuation of SA and SE growth combined with a weak (3 day^{-1}) and short (2 days) SA-killing, for instance, improved the success rate from 0 to 70% for all irreversible virtual skin sites (Figures 5c and 3c) and 30 to 90% for all reversible virtual skin sites (Figures 5d and 3d) in the model. Furthermore, a strong enough attenuation of SA and SE growth could even make damaged skin states disappear altogether (Figure 5f), explaining why a 56% recovery of all damaged virtual skin sites was observed even for 0 $days^{-1}$ strength of a simulated SA-killing treatment (Figure 5b).

However, simulations of the dual-action treatment with stronger attenuation of SE than of SA caused some reversible virtual skin sites to lose their non-damaged skin state (Supplementary Figure S6d). Enhancing the model parameter describing SE growth attenuation for virtual skin sites colonized by non-skin-damaging SE could weaken SE's ability to control SA populations through its QS products, resulting in skin damage by SA. This observation highlights the importance of attenuating both SA and SE growths similarly *in silico* rather than focusing on one species or the other.

DISCUSSION

In silico analysis reveals the model interactions driving the emergence of skin damaging SA–SE populations

SA is almost always found in AD skin lesions and can cause skin damage. However, SE, which can control SA, is also prevalent (Byrd et al, 2017; Kong et al, 2012; Rauer et al, 2023). In this study, we developed and analyzed an *in silico* model of AD lesions with SA–SE colonization and found that the key interaction parameters that allow the emergence of a damaged skin state in a virtual skin site represent a weak attenuation of SA and SE growth and slow skin desquamation and repair. From these results, we hypothesize that poor skin physiology in AD skin lesions may allow SA to grow to skin-damaging populations, even if SE can kill SA and inhibit its virulence.

The *in silico* model suggested that SA and SE can also coexist in a non-damaged skin state if the model parameters represent a strong attenuation of SA and SE growth and fast skin desquamation and repair. If such AD skin sites exist in the clinic, one may observe the existence of SA as a commensal phenotype (Krismer et al, 2017) with inactive QS. However, SA may proliferate to skin-damaging populations if the skin loses its ability to control bacterial growth, for example, due to loss of the acid mantle in AD (Panther and Jacob, 2015) or change in host antimicrobial peptide production (Nakatsuji et al, 2023). Thus, a possible route for AD pathogenesis may be the weakening of skin function, followed by the overgrowth and skin damaging by pre-existing populations of SA and/or SE, hidden as commensal phenotypes, suggesting that microbial dysbiosis in AD may be a type of epiphenomenon.

In silico simulations suggest promising treatment strategy

We explored how *in silico* treatments could recover damaged virtual skin sites to a non-damaged state. To determine a widely applicable treatment, we simulated the treatment to a vast number of different virtual skin sites, each defined by a unique set of parameters representing different skin physiologies and bacterial properties.

The first treatment simulated the killing of only SA. This treatment was previously predicted to be promising (Miyano et al, 2022), but its efficacy beyond the treatment period or in

the presence of a skin-damaging CoNS was unclear. In this study, we investigated the long-term efficacy of a simulated temporary SA-killing by evaluating whether treated damaged skin sites could eventually converge to a non-damaging skin state. The simulated SA-killing treatment performed poorly, largely because SA-killing failed on irreversible virtual skin sites that did not have a non-damaged state to converge to. In our model simulation, SA-killing only perturbs SA populations, which sometimes enable the overgrowth of SE to continue damaging skin.

We then proposed an alternative dual-action treatment inspired by the characteristics of asymptomatic virtual skin sites in the model because they only converge to a non-damaged skin state. The dual-action treatment involved applying a continuous enhancement of SA and SE growth attenuation together with temporary SA-killing, which *in silico* simulations showed increased the proportion of all damaged virtual skin sites that recovered to a non-damaged skin state, even with a relatively short and weak SA-killing. Its success was attributed to the increase in model parameter values representing SA and SE growth attenuation that enabled the emergence of a non-damaged skin state, even for irreversible virtual skin sites.

On the basis of these *in silico* model results, we speculate that temporary SA-killing in the clinic will not prevent SA recolonization, for example, from transmission and regrowing to a skin damaging phenotype. AD is indeed characterized by poor skin function and control of SA growth in the clinic, with patients having higher skin pH (Geoghegan et al, 2018; Lambers et al, 2006; Panther and Jacob, 2015), lower host antimicrobial peptide concentration (Ong et al, 2002; Sieprawska-Lupa et al, 2004), and reduced skin microbiome diversity (Byrd et al, 2017; Clausen et al, 2018; Kong et al, 2012). We hypothesize that the dual-action treatment strategy applied in clinical practice may be more efficacious and widely appliable than SA-killing alone as predicted by the *in silico* model. The promise of the dual-action treatment strategy in the clinic is supported by a previous study (Miyano et al, 2022) that revealed that the efficacy of SA-killing was potentiated if administered in conjunction with dupilumab, a biologic that indirectly enhances skin barrier integrity by inhibiting IL-4 and IL-13 receptors.

Moving to validation of the proposed treatment with future clinical studies

The *in silico* model developed in this study is a mathematical description of the current working knowledge of the interactions between SA and SE, and how they exacerbate skin damage in AD lesions, on the basis of literature and key assumptions of the biology. The full applicability of the model cannot be established until a study is done in the future to validate the model predictions in collaboration with clinicians. This could further improve the model and its utility to elucidate basic biology, advance understanding of the disease, and optimize successful treatment strategies.

We envision that validation of the dual-action treatment regime proposed in this study could be confirmed in the laboratory. For instance, one could culture SA and SE on an organotypic skin model (Rikken et al, 2023) at pH 7 (to mimic the higher pH environment on AD lesions [Sparavigna et al, 1999]) in 3 conditions: (i) without any treatment; (ii) application of SA-killing only, enacted through the temporal addition of PSM γ harvested from SE (Cogen et al, 2010); and (iii) application of the dual-action treatment enacted by the temporal addition of PSM γ (SA-killing) and application of a hydrochloric acid cream of pH 3.5 to attenuate SA and SE growths (Iyer et al, 2021; Lee et al, 2016). The validity of the dual-action treatment would be confirmed in the laboratory if we observe lower steady state abundances of SA and/or SE and no expression of SA or SE QS−induced agr P3 promoter (Jenul and Horswill, 2019; Olson et al, 2014), that is, no damage to the organotypic skin model, compared with only SA-killing. We envision that this *in vitro* validation will pave the route to a similar validation in mouse and human clinical studies.

A potential limitation of applying the acid cream for the dual-action treatment is not knowing how frequently or for how long it should be applied to a patient in the clinic. The *in silico* model suggests that growth attenuation needs to be applied indefinitely. However, the dual-action treatment implemented in the clinic may allow recovery of the skin and/or re-emergence of diverse skin commensals, which may continue the attenuation of SA and SE growth and allow treatment to be stopped. For instance, improvements in AD symptoms by standard AD treatments (eg, emollients and corticosteroids) were reported to be correlated with the re-establishment of a more diverse skin microbiome with reduced SA prevalence (Khadka et al, 2021), suggesting that increasing the skin microbiome diversity is crucial for long-term recovery from AD. We speculate that the dual-action treatment proposed in this study may be necessary only until skin commensals re-emerge on AD skin to provide synergistic control on SA and SE growth and reinforce the skin barrier integrity (Byrd et al, 2017; Zheng et al, 2022). We envision that clinical studies will help to determine the optimal duration of acid cream application until microbiome re-establishment.

It is unclear how other commensals would be affected by the application of an acid cream, although SA may be more strongly attenuated than SE (Iyer et al, 2021). We speculate that the application of a pH 3.5 dilute hydrochloric acid cream may enable other skin commensals to thrive at higher relative abundances as they do in healthy skin (Byrd et al, 2017; Kong et al, 2012) because this cream reportedly maintained a skin surface pH of 4.5−5 (Lee et al, 2016), close to a healthy skin pH (Panther and Jacob, 2015). We effectively simulated the worst case scenario outcomes from the dual-action treatment by modelling only the interactions between SA, SE, and the skin barrier while neglecting the potential added inhibition of SA and SE growths by an increased abundance of commensals during recovery. We envision that the effects of the acid cream on SA, SE, and other skin microbiota would be established from clinical studies in the future.

Future uses of the model to address assumptions of the basic biology of AD

In this study, we developed an *in silico* model of a virtual skin site describing the interactions between SA, SE, and the skin

barrier. We chose to model SA and SE because several studies have consistently found that they are the 2 most abundant species in AD lesions, whereas the abundance of other commensal species appear to be less consistent across samples (Byrd et al, 2017; Kong et al, 2012; Nakatsuji et al, 2021, 2017; Rauer et al, 2023). Furthermore, SA and SE have been shown to contribute to skin damage (Cau et al, 2021; Tian et al, 2021). We appreciate that there is a wide heterogeneity of microbiomes in AD skin lesions and that the other commensals we chose not to model may play a role in controlling SA and SE populations (Nakatsuji et al, 2021, 2017). For the purposes of this study, we assumed that the contribution of all other skin commensals to controlling SA and/or SE are negligible because they are typically in low relative abundance in AD lesions (Byrd et al, 2017; Kong et al, 2012; Rauer et al, 2023). Validating the model with time-course data of microbial absolute abundances and barrier integrity measurements from clinical patients would improve the model's predictive power and enhance our understanding of the relative contribution of SA and SE against commensals in AD pathogenesis. Despite an absence of SA−SE dynamic data in the literature, as far as we are aware, the model could still uncover 2 key qualitative features of SA−SE steady state compositions reported in previous studies: the stable coexistence of SA and SE in some patients and the dominance of SA or SE in other patients (Byrd et al, 2017; Cau et al, 2021; Kong et al, 2012).

After model validation, the *in silico* model could be used to address assumptions of the biology of AD. For example, it is assumed that SA can grow to skin-damaging populations and prevent recovery of the skin after a large enough initial damage to the skin barrier, for example, by injury (Wanke et al, 2013). To elucidate whether and how large an initial damage would allow SA to prevent the skin from recovering, one could use the *in silico* model to simulate the skin barrier integrity reached from different levels of initial skin damage. As another example, SA is commonly the dominant species in AD skin lesions (Byrd et al, 2017; Kong et al, 2012; Rauer et al, 2023) and is assumed to kill its competitor SE to become dominant. To establish whether it is necessary for SA to kill SE to become dominant, the model can be used to determine which species eventually dominates at steady state if SA cannot kill SE compared with if it can.

Beyond the basic biology, the validated *in silico* model could be used to suggest optimal treatment regimes. Treatment optimization can be posed as a multi-objective optimization problem to maximize the proportion of damaged virtual skin sites that recover to a non-damaged skin state but minimize the total amount and length of treatment applied in the model. It is then crucial for the optimal treatment regime to be tested in laboratory or clinical studies to confirm whether the treatment strength and duration identified by the model can be feasibly attained.

The *in silico* model has not accounted for potential antagonism or synergism between the treatments enacting SA-killing and bacterial growth attenuation. Determining their interactions experimentally will allow us to incorporate them into the model, enabling a more accurate prediction of the treatment outcome *in silico* and helping optimize the proposed dual-action treatment to maximize treatment success rate.

This study demonstrates that *in silico* modeling can be used to help unveil the key mechanisms driving a system to a damaged skin state. Persistent AD lesions in our model are characterized by parameters describing a poor attenuation of SA growth by the skin and slow desquamation. Identifying the key mechanisms leading to the emergence of an asymptomatic virtual skin site with a single non-damaged skin state helped to inspire a promising dual-action treatment strategy in our *in silico* model of AD lesions with SA−SE colonization. The *in silico* investigation suggests that enhancing the skin's attenuation of SA and SE growth can enable SA-killing to recover a non-damaged skin state for many virtual skin sites, including those with a skin-damaging SE. The results from this *in silico* study need to be confirmed in clinical settings but show promise to be widely applicable. We believe that this model provides a powerful tool for investigative dermatology by enabling a rational proposal of treatments through understanding how SA−SE−skin interactions may be contributing to AD pathogenesis.

MATERIALS AND METHODS

Model overview

The proposed *in silico* model of AD lesions with SA−SE colonization is defined by 3 ordinary differential equations:

$$\frac{dA}{dt} = \frac{\kappa_A \cdot A(t)}{1+\gamma_{AB}\cdot B(t)}\left(1-\frac{A(t)}{A_{max}}\right)-\delta_{AE}\cdot\frac{sw_E\cdot E(t)}{sw_E\cdot E(t)+\widehat{E}_{p,th}}\cdot A(t)-\delta_B\cdot A(t), \tag{1}$$

$$\frac{dE}{dt} = \frac{\kappa_E \cdot E(t)}{1+\gamma_{EB}\cdot B(t)}\left(1-\frac{E(t)}{E_{max}}\right)-\delta_{EA}\cdot\frac{sw_A\cdot A(t)}{sw_A\cdot A(t)+\widehat{A}_{p,th}}\cdot E(t)-\delta_B\cdot E(t), \tag{2}$$

$$\frac{dB}{dt} = \kappa_B\cdot(1-B(t))-\widehat{\delta}_{BE}\cdot sw_E(E)\cdot E(t)\cdot B(t)-\widehat{\delta}_{BA}\cdot sw_A(A)\cdot A(t)\cdot B(t), \tag{3}$$

Where t is time (days), $A(t)$ and $E(t)$ are the bacterial population densities (colony-forming unit/cm^2) of SA and SE on the skin, and $B(t)$ is the skin barrier integrity (unitless). We set $A(t)$ and $E(t)$=0 when their respective populations become <1 colony-forming unit/cm^2 because bacterial population densities measured in colony-forming unit/cm^2 are integers. $B(t)$=0 represents complete barrier damage, and $B(t)$=1 represents the skin barrier without damage.

As the populations of SA and SE grow, small amounts of AIPs are secreted from each species and activate a QS-switch of the agr in *Staphylococci* to synthesize antimicrobial peptides and virulence factors. We model the AIP-induced QS-switches as Heaviside functions:

$$sw_A(A) = \begin{cases} 0, & 0 < A < \widehat{A}_{th}\cdot(1+\widehat{\gamma}_{AE}\cdot sw_E(E)\cdot E), \\ 1, & A \geq \widehat{A}_{th}\cdot(1+\widehat{\gamma}_{AE}\cdot sw_E(E)\cdot E), \end{cases} \tag{4}$$

$$sw_E(E) = \begin{cases} 0, & 0 < E < \widehat{E}_{th}, \\ 1, & E \geq \widehat{E}_{th}, \end{cases} \quad (5)$$

Where $\widehat{A}_{th}$ and $\widehat{E}_{th}$ denote the threshold population sizes of SA and SE that result in the switch on of QS, and $\widehat{\gamma}_{AE}$ describes the strength at which SE inhibits SA virulence factor production.

Steady state analysis

Steady states are defined in this study as the values of SA, SE, and skin barrier integrity (A^*, E^*, B^*) when $\max(|dA/dt|, |dE/dt|, |dB/dt|) \leq 10^{-6}$. Steady states are stable when the eigenvalues of their Jacobian matrix evaluated at a particular steady state have negative real parts.

We derived the stable steady states for each parameter set using analytical and numerical approaches. When at least 1 QS-switch is inactive, we obtained analytical solutions for 8 of 9 steady states of SA, SE, and skin barrier integrity (A^*, E^*, B^*) using simultaneous equations (Supplementary Materials and Methods) because the 3 ordinary differential equations (ODEs) for SA, SE, and skin barrier integrity are decoupled. When both QS-switches are on, an analytical solution could not be obtained owing to interlinking variables, and we adopted a numerical approach with MATLAB ODE solver function ode15s for numeric integration of stiff systems. We performed time-course simulations using the maximum population sizes of SA (A_{max}) and SE (E_{max}) as the initial conditions and simulated until steady states are reached. We do not consider the time taken to converge to a stable steady state in our model analyses.

Computational simulations of treatment application

We used MATLAB ode15s to simulate the effects of treatment applications and reported the steady states at 10^6 days after the treatment was removed. The initial conditions are damaged skin states of irreversible and reversible virtual skin sites. We chose the damaged skin state with large populations of SA (ie, its QS-switch was active) as the initial state if it existed for a particular virtual skin site. For the virtual skin sites with more than 1 damaged skin state with large SA populations, we chose the SA-driven damaged skin state (where its QS-switch is active) with the lowest barrier integrity because it represents the worst skin condition. If large populations of SA did not exist for a particular virtual skin site, we started the simulation from a damaged skin state driven by large SE populations with an active QS-switch. This is because we assume that clinicians treat patients with AD on the basis of whether a damaged state is observed without an easy method to distinguish whether skin damage is caused by SA or SE.

We describe the effects of SA-killing by adding a term for SA-killing with a rate δ_{AS} [day^{-1}]:

$$\frac{dA}{dt} = \frac{\kappa_A \cdot A(t)}{1 + \gamma_{AB} \cdot B(t)} \left(1 - \frac{A(t)}{A_{max}}\right) - \delta_{AE} \cdot \frac{sw_E \cdot E(t)}{sw_E \cdot E(t) + \widehat{E}_{p,th}} \cdot A(t) - \delta_B \cdot A(t) - \delta_{AS} \cdot A(t) \quad (6)$$

We explored different strengths (δ_{AS}) and durations of SA-killing and reported the stable steady state the system converged to at 10^6 days from treatment removal.

The proposed dual-action treatment involves a continuous enhancement of bacterial growth attenuation by the skin (with the fold-change increase described by γ_{AS} and γ_{ES}) and temporary SA-killing:

$$\frac{dA}{dt} = \frac{\kappa_A \cdot A(t)}{1 + \gamma_{AS} \cdot \gamma_{AB} \cdot B(t)} \left(1 - \frac{A(t)}{A_{max}}\right) - \delta_{AE} \cdot \frac{sw_E \cdot E(t)}{sw_E \cdot E(t) + \widehat{E}_{p,th}} \cdot A(t) - \delta_B \cdot A(t) - \delta_{AS} \cdot A(t) \quad (7)$$

$$\frac{dE}{dt} = \frac{\kappa_E \cdot E(t)}{1 + \gamma_{ES} \cdot \gamma_{EB} \cdot B(t)} \left(1 - \frac{E(t)}{E_{max}}\right) - \delta_{EA} \cdot \frac{sw_A \cdot A(t)}{sw_A \cdot A(t) + \widehat{A}_{p,th}} \cdot E(t) - \delta_B \cdot E(t) \quad (8)$$

A continuous enhancement of bacterial growth attenuation changes the number and type of stable steady states seen for a particular virtual skin site. We recalculated the stable steady states for each virtual skin site with varying strengths of bacterial growth attenuation ($1 \leq \gamma_{AS} \leq 30$ and $1 \leq \gamma_{ES} \leq 30$). We simulated a fixed SA-killing for a range of bacterial growth attenuation strengths, starting from the damaged stable states observed after SA and SE growth attenuation was applied.

All computational analysis was performed using MATLAB (version R2021b; MathWorks).

ETHICS STATEMENT

The study in this manuscript is exclusively computational and does not contain any human or animal studies.

DATA AVAILABILITY STATEMENT

The code related to this article can be found at GitHub at https://github.com/jamie-852/SASE-model.

ORCIDs

Jamie Lee: http://orcid.org/0000-0001-8314-6651
Ahmad A. Mannan: http://orcid.org/0000-0001-7628-8416
Takuya Miyano: http://orcid.org/0000-0002-1181-6924
Alan D. Irvine: http://orcid.org/0000-0002-9048-2044
Reiko J. Tanaka: http://orcid.org/0000-0002-0769-9382

CONFLICT OF INTEREST

TM reports personal fees from Daiichi Sankyo, during the conduct of the study, outside of the submitted work. ADI reports personal fees from Sanofi Regeneron, AbbVie, Eli Lilly, Pfizer, UCB Pharma, Novartis, Dermavant, Benevolent AI, Menlo Therapeutics, Chugai, LEO Pharma, and Arena during the conduct of the study. The remaining authors state no conflict of interest.

ACKNOWLEDGMENTS

This work was funded by the EPSRC as part of the Centre for Doctoral Training in BioDesign Engineering (EP/S022856/1) and by the Innovate UK and the EIC pathfinder (SKINDEV Skin microbial devices, 101098826).

AUTHOR CONTRIBUTIONS

Conceptualization: JL, AAM, TM, RJT; Data Curation: JL, AAM, TM, Formal Analysis: JL, AAM, TM; Funding Acquisition: RJT; Investigation: JL, AAM, TM; Methodology: JL, AAM, TM; Software: JL; Supervision: RJT; Validation: AAM, RJT; Visualization: JL, AAM, RJT; Writing − Original Draft Preparation: JL, AAM, RJT; Writing − Review and Editing: JL, AAM, TM, AI, RJT

DECLARATION OF GENERATIVE ARTIFICIAL INTELLIGENCE (AI) OR LARGE LANGUAGE MODELS (LLMs)

No generative AI or LLMs were used in the writing process.

SUPPLEMENTARY MATERIAL

Supplementary material is linked to the online version of the paper at www.jidonline.org, and at https://doi.org/10.1016/j.jid.2024.100269.

REFERENCES

Asher MI, Montefort S, Björkstén B, Lai CK, Strachan DP, Weiland SK, et al. Worldwide time trends in the prevalence of symptoms of asthma, allergic

rhinoconjunctivitis, and eczema in childhood: ISAAC Phases One and Three repeat multicountry cross-sectional surveys. Lancet 2006;368:733–43.

Bjerre RD, Holm JB, Palleja A, Sølberg J, Skov L, Johansen JD. Skin dysbiosis in the microbiome in atopic dermatitis is site-specific and involves bacteria, fungus and virus. BMC Microbiol 2021;21:256.

Byrd AL, Deming C, Cassidy SKB, Harrison OJ, Ng WI, Conlan S, et al. Staphylococcus aureus and staphylococcus epidermidis strain diversity underlying pediatric atopic dermatitis. Sci Transl Med 2017;9:eaal4651.

Cau L, Williams MR, Butcher AM, Nakatsuji T, Kavanaugh JS, Cheng JY, et al. Staphylococcus epidermidis protease EcpA can be a deleterious component of the skin microbiome in atopic dermatitis. J Allergy Clin Immunol 2021;147:955–66.e16.

Clausen ML, Agner T, Lilje B, Edslev SM, Johannesen TB, Andersen PS. Association of disease severity with skin microbiome and filaggrin gene mutations in adult atopic dermatitis. JAMA Dermatol 2018;154:293–300.

Cogen AL, Yamasaki K, Sanchez KM, Dorschner RA, Lai Y, MacLeod DT, et al. Selective antimicrobial action is provided by phenol-soluble modulins derived from staphylococcus epidermidis, a normal resident of the skin. J Invest Dermatol 2010;130:192–200.

Elias PM. The how, why and clinical importance of stratum corneum acidification. Exp Dermatol 2017;26:999–1003.

Fournière M, Latire T, Souak D, Feuilloley MGJ, Bedoux G. Staphylococcus epidermidis and Cutibacterium acnes: two major sentinels of skin microbiota and the influence of cosmetics. Microorganisms 2020;8:1752.

Geoghegan JA, Irvine AD, Foster TJ. Staphylococcus aureus and atopic dermatitis: a complex and evolving relationship. Trends Microbiol 2018;26:484–97.

Hardy BL, Bansal G, Hewlett KH, Arora A, Schaffer SD, Kamau E, et al. Antimicrobial activity of clinically isolated bacterial species against Staphylococcus aureus. Front Microbiol 2020;10:2977.

Hoffman DR, Kroll LM, Basehoar A, Reece B, Cunningham CT, Koenig DW. Immediate and extended effects of sodium lauryl sulphate exposure on stratum corneum natural moisturizing factor. Int J Cosmet Sci 2014;36:93–101.

Hwang J, Thompson A, Jaros J, Blackcloud P, Hsiao J, Shi VY. Updated understanding of Staphylococcus aureus in atopic dermatitis: from virulence factors to commensals and clonal complexes. Exp Dermatol 2021;30:1532–45.

Iyer V, Raut J, Dasgupta A. Impact of pH on growth of staphylococcus epidermidis and staphylococcus aureus in vitro. J Med Microbiol 2021:70.

James EH, Edwards AM, Wigneshweraraj S. Transcriptional downregulation of agr expression in Staphylococcus aureus during growth in human serum can be overcome by constitutively active mutant forms of the sensor kinase AgrC. FEMS Microbiol Lett 2013;349:153–62.

Jenul C, Horswill AR. Regulation of Staphylococcus aureus virulence. Microbiol Spectr 2019;7. https://doi.org/10.1128/microbiolspec.GPP3-0031-2018.

Khadka VD, Key FM, Romo-González C, Martínez-Gayosso A, Campos-Cabrera BL, Gerónimo-Gallegos A, et al. The skin microbiome of patients with atopic dermatitis normalizes gradually during treatment. Front Cell Infect Microbiol 2021;11:720674.

Kong HH, Oh J, Deming C, Conlan S, Grice EA, Beatson MA, et al. Temporal shifts in the skin microbiome associated with disease flares and treatment in children with atopic dermatitis. Genome Res 2012;22:850–9.

Koster MI. Making an epidermis. Ann N Y Acad Sci 2009;1170:7–10.

Krismer B, Weidenmaier C, Zipperer A, Peschel A. The commensal lifestyle of Staphylococcus aureus and its interactions with the nasal microbiota. Nat Rev Microbiol 2017;15:675–87.

Lambers H, Piessens S, Bloem A, Pronk H, Finkel P. Natural skin surface pH is on average below 5, which is beneficial for its resident flora. Int J Cosmet Sci 2006;28:359–70.

Langan SM, Irvine AD, Weidinger S. Atopic dermatitis. Lancet 2020;396:345–60.

Lee NR, Lee HJ, Yoon NY, Kim D, Jung M, Choi EH. Application of topical acids improves atopic dermatitis in murine model by enhancement of skin barrier functions regardless of the origin of acids. Ann Dermatol 2016;28:690–6.

Miajlovic H, Fallon PG, Irvine AD, Foster TJ. Effect of filaggrin breakdown products on growth of and protein expression by Staphylococcus aureus. J Allergy Clin Immunol 2010;126:1184–90.e3.

Miyano T, Irvine AD, Tanaka RJ. Model-based meta-analysis to optimize Staphylococcus aureus–targeted therapies for atopic dermatitis. JID Innov 2022;2:100110.

Nakagawa S, Matsumoto M, Katayama Y, Oguma R, Wakabayashi S, Nygaard T, et al. Staphylococcus aureus virulent PSMα peptides induce keratinocyte alarmin release to orchestrate IL-17-dependent skin inflammation. Cell Host Microbe 2017;22:667–77.e5.

Nakamura Y, Oscherwitz J, Cease KB, Chan SM, Muñoz-Planillo R, Hasegawa M, et al. Staphylococcus δ-toxin induces allergic skin disease by activating mast cells. Nature 2013;503:397–401.

Nakatsuji T, Brinton SL, Cavagnero KJ, O'Neill AM, Chen Y, Dokoshi T, et al. Competition between skin antimicrobial peptides and commensal bacteria in type 2 inflammation enables survival of S. aureus. Cell Rep 2023;42:112494.

Nakatsuji T, Chen TH, Narala S, Chun KA, Two AM, Yun T, et al. Antimicrobials from human skin commensal bacteria protect against Staphylococcus aureus and are deficient in atopic dermatitis. Sci Transl Med 2017;9:eaah4680.

Nakatsuji T, Chen TH, Two AM, Chun KA, Narala S, Geha RS, et al. Staphylococcus aureus exploits epidermal barrier defects in atopic dermatitis to trigger cytokine expression. J Invest Dermatol 2016;136:2192–200.

Nakatsuji T, Hata TR, Tong Y, Cheng JY, Shafiq F, Butcher AM, et al. Development of a human skin commensal microbe for bacteriotherapy of atopic dermatitis and use in a phase 1 randomized clinical trial. Nat Med 2021;27:700–9.

Nutten S. Atopic dermatitis: global epidemiology and risk factors. Ann Nutr Metab 2015;66:8–16.

Olson ME, Todd DA, Schaeffer CR, Paharik AE, Van Dyke MJ, Büttner H, et al. Staphylococcus epidermidis agr quorum-sensing system: signal identification, cross talk, and importance in colonization. J Bacteriol 2014;196:3482–93.

Ong PY, Ohtake T, Brandt C, Strickland I, Boguniewicz M, Ganz T, et al. Endogenous antimicrobial peptides and skin infections in atopic dermatitis. N Engl J Med 2002;347:1151–60.

Otto M, Echner H, Voelter W, Götz F. Pheromone cross-inhibition between Staphylococcus aureus and Staphylococcus epidermidis. Infect Immun 2001;69:1957–60.

Palmer CNA, Irvine AD, Terron-Kwiatkowski A, Zhao Y, Liao H, Lee SP, et al. Common loss-of-function variants of the epidermal barrier protein filaggrin are a major predisposing factor for atopic dermatitis. Nat Genet 2006;38:441–6.

Panther DJ, Jacob SE. The importance of acidification in atopic eczema: an underexplored avenue for treatment. J Clin Med 2015;4:970–8.

Rauer L, Reiger M, Bhattacharyya M, Brunner PM, Krueger JG, Guttman-Yassky E, et al. Skin microbiome and its association with host cofactors in determining atopic dermatitis severity. J Eur Acad Dermatol Venereol 2023;37:772–82.

Rikken G, Meesters LD, Jansen PAM, Rodijk-Olthuis D, van Vlijmen-Willems IMJJ, Niehues H, et al. Novel methodologies for host-microbe interactions and microbiome-targeted therapeutics in 3D organotypic skin models. Microbiome 2023;11:227.

Sieprawska-Lupa M, Mydel P, Krawczyk K, Wójcik K, Puklo M, Lupa B, et al. Degradation of human antimicrobial peptide LL-37 by Staphylococcus aureus-derived proteinases. Antimicrob Agents Chemother 2004;48:4673–9.

Sparavigna A, Setaro M, Gualandri V. Cutaneous pH in children affected by atopic dermatitis and in healthy children: A multicenter study. Ski Res Technol 1999;5:221–7.

Tanaka RJ, Ono M. Skin disease modeling from a mathematical perspective. J Invest Dermatol 2013;133:1472–8.

Teichmann P, Both A, Wolz C, Hornef MW, Rohde H, Yazdi AS, et al. The Staphylococcus epidermidis transcriptional profile during carriage. Front Microbiol 2022;13:896311.

Tian X, Huang Q, Liang J, Wang J, Zhang J, Yang Y, et al. A review of the mechanisms of keratinocytes damage caused by Staphylococcus aureus

infection in patients with atopic dermatitis. J Leukoc Biol 2021;110:1163–9.

Toribio A, Martínez-Blanco H, Rodríguez-Aparicio L, Ferrero MÁ, Marrodán T, Fernández-Natal I. In vitro adherence of conjunctival bacteria to different oculoplastic materials. Int J Ophthalmol 2018;11:1895–901.

Wanke I, Skabytska Y, Kraft B, Peschel A, Biedermann T, Schittek B. Staphylococcus aureus skin colonization is promoted by barrier disruption and leads to local inflammation. Exp Dermatol 2013;22:153–5.

Williams MR, Costa SK, Zaramela LS, Khalil S, Todd DA, Winter HL, et al. Quorum sensing between bacterial species on the skin protects against epidermal injury in atopic dermatitis. Sci Transl Med 2019;11:eaat8329.

Williams MR, Nakatsuji T, Sanford JA, Vrbanac AF, Gallo RL. Staphylococcus aureus induces increased serine protease activity in keratinocytes. J Invest Dermatol 2017;137:377–84.

Zheng Y, Hunt RL, Villaruz AE, Fisher EL, Liu R, Liu Q, et al. Commensal Staphylococcus epidermidis contributes to skin barrier homeostasis by generating protective ceramides. Cell Host Microbe 2022;30:301–13.e9.

Zhou W, Spoto M, Hardy R, Guan C, Fleming E, Larson PJ, et al. Host-specific evolutionary and transmission dynamics shape the functional diversification of Staphylococcus epidermidis in human skin. Cell 2020;180:454–70.e18.

SUPPLEMENTARY RESULTS

Subcategorization of virtual skin sites of atopic dermatitis lesions with *Staphylococcus aureus*–*Staphylococcus epidermidis* colonization

We subcategorized the 3 types of virtual skin sites—asymptomatic, reversible, and irreversible—on the basis of the populations of *Staphylococcus aureus* (SA) and *Staphylococcus epidermidis* (SE) and how many stable states were present (Supplementary Figure S1), demonstrating that although many subtypes exist, they all belong to 1 of the 3 defined virtual skin types.

Effects of SA-killing treatment

We explored the effectiveness of the SA-killing treatment over long durations (maximum of 50 days) and strengths (maximum of 10 days^{-1}) (Supplementary Figure S2) to see whether an improved rate of treatment success could be observed when compared with shorter durations and weaker treatments. In addition, we found that some reversible skin sites with skin-damaging SE required a precise treatment regimen to converge to a non-damaged skin state in the model after SA-killing treatment was removed (Supplementary Figure S3).

Analysis of parameters driving asymptomatic, reversible, and irreversible skin sites

When analyzing the parameters driving asymptomatic, reversible, or irreversible skin sites, we plotted the distribution of all parameter values for each category as violin plots (Supplementary Figure S4) and then extracted the key parameters that were qualitatively different when comparing between the 3 types of virtual skin sites. Furthermore, we analyzed the effects of skin-damaging SE strains on the mechanisms driving asymptomatic, reversible, and irreversible skin sites by splitting virtual skin sites on the basis of whether they had skin damaging or non-damaging strains of SE (Supplementary Figure S5).

Effects of enhancing SA and SE growth attenuation

In the implementation of the dual-action treatment, we found that increasing levels of growth attenuation of SA and SE allows SA-killing to recover a larger percentage of virtual skin sites to a non-damaged skin state (Supplementary Figure S6a). Enhancing SA and SE growth attenuation evenly and strongly enables the largest percentage of damaged skin sites to gain a non-damaged skin state (Supplementary Figure S6b–d).

SUPPLEMENTARY MATERIALS AND METHODS

Model parameters

The nominal value of each parameter defined in Supplementary Table S1 was either derived from published data (9 parameters discussed in the section titled derivation of parameters from published data) or chosen arbitrarily (the remaining 8 parameters discussed in the section titled motivation for how the remaining parameter values were chosen). Parameter values were derived by either (i) directly extracting data points from previously published papers or (ii) fitting model equations to extracted data points by a least-squares fit. Data points were extracted from published papers using WebPlotDigitizer (Rohatgi, 2022).

Model construction

Overview of the simplified* in silico *model. We show the model schematic (Supplementary Figure S7) and the simplified model equations describing AD lesional skin with SA–SE colonization in this section.

For SA growth, death, and its quorum sensing (QS) autoinducing peptide (AIP)–induced weaponization, we used the following:

Population growth

$$\frac{dA}{dt} = \frac{\kappa_A \cdot A}{1+\gamma_{AB}\cdot B}\left(1-\frac{A}{A_{max}}\right)\ldots$$

Population death

$$\ldots - \delta_{AE}\cdot\frac{sw_E\cdot E}{sw_E\cdot E+\widehat{E}_{p,th}}\cdot A - \delta_B\cdot A,$$

AIP-induced QS-switch

$$sw_A(A) = \begin{cases} 0, & 0 < A < \widehat{A}_{th}\cdot(1+\widehat{\gamma}_{AE}\cdot sw_E(E)\cdot E), \\ 1, & A \geq \widehat{A}_{th}\cdot(1+\widehat{\gamma}_{AE}\cdot sw_E(E)\cdot E), \end{cases}$$

For SE growth, death, and its QS AIP-induced weaponization, we used the following:

Population growth

$$\frac{dE}{dt} = \frac{\kappa_E\cdot E}{1+\gamma_{EB}\cdot B}\left(1-\frac{E}{E_{max}}\right)\ldots$$

Population death

$$\ldots - \delta_{EA}\cdot\frac{sw_A\cdot A}{sw_A\cdot A+\widehat{A}_{p,th}}\cdot E - \delta_B\cdot E,$$

AIP-induced QS-switch

$$sw_E(E) = \begin{cases} 0, & 0 < E < \widehat{E}_{th}, \\ 1, & E \geq \widehat{E}_{th}. \end{cases}$$

For skin barrier integrity, we used the following:

Skin barrier maintenance and repair and damage by microbial virulence factors

$$\frac{dB}{dt} = \kappa_B\cdot(1-B) - \widehat{\delta}_{BE}\cdot sw_E(E)\cdot E\cdot B\ldots$$
$$\ldots - \widehat{\delta}_{BA}\cdot sw_A(A)\cdot A\cdot B$$

Overview of full* in silico *model. We show the full model equations describing AD lesional skin with SA–SE colonization in this section, which simplifies to the model equations presented earlier through the steps outlined in the section on model structure and underlying assumptions which helped simplify the full model.

For SA growth, death, and its QS AIP-induced weaponization, we used the following:

SA dynamics

$$\frac{dA}{dt} = \frac{\kappa_A \cdot A}{1 + \gamma_{AB} \cdot B}\left(1 - \frac{A}{A_{max}}\right) - \delta_{AE} \cdot \frac{E_p}{E_p + E_{p,th}} \cdot A - \delta_B \cdot A,$$

SA AIP-induced QS-switch

$$sw_A(A_I) = \begin{cases} 0, & 0 < A_I < A_{I,th} \cdot (1 + \gamma_{AE} \cdot E_I), \\ 1, & A_I \geq A_{I,th} \cdot (1 + \gamma_{AE} \cdot E_I), \end{cases}$$

SA AIP dynamics

$$\frac{dA_I}{dt} = (r_{AI,min} + r_{AI,max} \cdot sw_A(A_I)) \cdot A - (\delta_{AI} + \delta_B) \cdot A_I,$$

SA antimicrobial peptide (AMP) dynamics

$$\frac{dA_p}{dt} = (r_{Ap} \cdot sw_A(A_I)) \cdot A - (\delta_{Ap} + \delta_B) \cdot A_p,$$

SA virulence factor dynamics

$$\frac{dA_{vf}}{dt} = (r_{Avf} \cdot sw_A(A_I)) \cdot A - (\delta_{Avf} + \delta_B) \cdot A_{vf}.$$

For SE growth, death, and its QS AIP-induced weaponization, we used the following:

SE dynamics

$$\frac{dE}{dt} = \frac{\kappa_E \cdot E}{1 + \gamma_{EB} \cdot B}\left(1 - \frac{E}{E_{max}}\right) - \delta_{EA} \cdot \frac{A_p}{A_p + A_{p,th}} \cdot E - \delta_B \cdot E,$$

SE AIP-induced QS-switch

$$sw_E(E_I) = \begin{cases} 0, & 0 < E_I < E_{I,th}, \\ 1, & E_I \geq E_{I,th}, \end{cases}$$

SE AIP dynamics

$$\frac{dE_I}{dt} = (r_{EI,min} + r_{EI,max} \cdot sw_E(E_I)) \cdot E - (\delta_{EI} + \delta_B) \cdot E_I,$$

SE AMP dynamics

$$\frac{dE_p}{dt} = (r_{Ep} \cdot sw_E(E_I)) \cdot E - (\delta_{Ep} + \delta_B) \cdot E_p,$$

SE virulence factor dynamics

$$\frac{dE_{vf}}{dt} = (r_{Evf} \cdot sw_E(E_I)) \cdot E - (\delta_{Evf} + \delta_B) \cdot E_{vf}.$$

For skin barrier integrity, we used the following:

Skin barrier maintenance and repair and damage by microbial virulence factors

$$\frac{dB}{dt} = \kappa_B \cdot (1 - B) - \delta_{BE} \cdot E_{vf} \cdot B - \delta_{BA} \cdot A_{vf} \cdot B.$$

Model structure and underlying assumptions that helped to simplify the full model

In this section, we discuss the structure of the ordinary differential equations (ODEs) modeling the dynamics of SA and SE growth, their population-dependent weaponization and battle, and their damage to the skin barrier integrity (Supplementary Figure S7), together with its underlying assumptions.

Growth of SA and SE populations. We model the growths of SA (A) and SE (E) populations with the following logistic growth equations:

$$\frac{dA(t)}{dt} = \frac{\kappa_A}{1 + \gamma_{AB} \cdot B(t)}\left(1 - \frac{A(t)}{A_{max}}\right)A(t), \quad \text{(S1)}$$

$$\frac{dE(t)}{dt} = \frac{\kappa_E}{1 + \gamma_{EB} \cdot B(t)}\left(1 - \frac{E(t)}{E_{max}}\right)E(t), \quad \text{(S2)}$$

Where parameters κ_A and κ_E represent the maximum growth rates, A_{max} and E_{max} represent the carrying capacities of each species, and γ_{AB} and γ_{EB} represent the degree to which the growth rates of each species is impaired when the barrier integrity is highest, that is, at $B = 1$. The model stands on 3 key assumptions:

Assumption 1: SA and SE grow on different carbon sources and do not compete for the same nutrients on AD skin. This assumption is based on the report that many microbes of the skin microbiota can grow on different carbon sources, even different strains of the same species (Timm et al, 2020).

Assumption 2: There is a maximum population capacity achievable for SA and SE on AD skin because it is understood that the skin flora is limited by competition for niche occupancy and limited nutrient availability on the skin (Elias, 2007).

Assumption 3: Decreases in the skin barrier integrity will allow faster growth of SA and SE populations. This is inferred from observations that on AD skin, SA and some strains of SE penetrate to deeper layers of the epidermis, where because of the higher pH environment there (Geoghegan et al, 2018), they are expected to grow faster and to higher population densities (Hülpüsch et al, 2020; Iyer et al, 2021). SA and SE breach and penetrate to deeper layers of the epidermis by traveling through the spaces between corneocytes and keratinocytes. Such space is created by the cleaving of corneodesmosomes and demosomes by the virulence factors and proteases secreted by SA and SE (Cau et al, 2021; Nakamura et al, 2013; Williams et al, 2017b).

Skin barrier recovery dynamics. We model the recovery of the skin barrier integrity according to the following:

$$\frac{dB}{dt} = \kappa_B \cdot (1 - B), \quad \text{(S3)}$$

Where parameter κ_B represents the maximum recovery rate.

Assumption 4: the skin has a natural capacity to achieve a full recovery from damage, and the dynamics of the barrier recovery is faster after greater damage to the skin and slower at lower damage. This is based on the observations of skin barrier recovery from exposures to damage by sodium lauryl sulphate reported in the study by Hoffman et al (2014).

SA and SE QS–mediated genetic switch. SA and SE can synthesize a multitude of peptides and protein-based armaments to support their colonization of the skin. Their expression is under the control of the *Staphylococcal* accessory gene regulator (agr) system (Jenul and Horswill, 2019), a 2-component QS system (Supplementary Figure S8). In brief, a signaling molecule called an AIP is synthesized and secreted at low levels into the environment through agrD–agrB. Once the bacteria population grows to a high density, the secreted AIPs accumulate to high enough densities to bind and be sensed by agrC. This then phosphorylates and activates cytosolic transcription factor agrA, which binds to 2 divergent promoters P2 and P3 to activate higher expressions of the products of the agrACDB and RNAIII regulons, namely, further AIPs and other armaments, including AMPs and virulence factors (Jenul and Horswill, 2019).

The AIPs are acting in a self-activating manner. A relatively small increase in its accumulation will lead to a large burst of AIPs, which in turn creates a strong activation of P2 and P3 expressions from its minimum to maximum rate. We model this AIP-induced nonlinear genetic switch in SA and SE as Heaviside functions of the AIPs:

$$\mathrm{sw}_A(A_I) = \begin{cases} 0, & 0 < A_I < A_{I,\mathrm{th}}, \\ 1, & A_I \geq A_{I,\mathrm{th}}, \end{cases} \tag{S4}$$

$$\mathrm{sw}_E(E_I) = \begin{cases} 0, & 0 < E_I < E_{I,\mathrm{th}}, \\ 1, & E_I \geq E_{I,\mathrm{th}}, \end{cases} \tag{S5}$$

Where parameters $A_{I,\mathrm{th}}$ and $E_{I,\mathrm{th}}$ represent the threshold concentrations of the AIPs of SA and SE at which their respective switch is activated.

SA and SE AIP expression. We model the dynamics of the expression of the AIPs of SA (A_I) and SE (E_I) as follows:

$$\frac{dA_I}{dt} = \left(r_{AI,\min} + r_{AI,\max} \cdot \mathrm{sw}_A(A_I)\right) \cdot A - (\delta_{AI} + \delta_B) \cdot A_I, \tag{S6}$$

$$\frac{dE_I}{dt} = \left(r_{EI,\min} + r_{EI,\max} \cdot \mathrm{sw}_E(E_I)\right) \cdot E - (\delta_{EI} + \delta_B) \cdot E_I, \tag{S7}$$

Where parameters $r_{*I,min}$ and $r_{*I,max}$ represent the basal and maximum expression rates, and δ_{*I} and δ_B represent the degradation rates and rate of loss by skin shedding. The non-zero low basal expressions of AIPs are required for the initial accumulation of AIPs before switching on the agr switch.

Assumption 5: the dynamics of the AIPs of SA and SE are at quasi-steady state. We have assumed that the relative timescales of the dynamics of AIPs is orders of magnitude lower (ie, faster) than parameters representing the growth of each species, their killing by AMPs from the other species, and species loss by skin desquamation. This assumption is based on several empirical studies (Junio et al, 2013; Mayville et al, 1999) that suggest that AIPs are relatively unstable. It has been speculated that AIPs should be rapidly inactivated *in vivo* because their AIP thiol-ester linkage can be hydrolyzed at physiological pH (Mayville et al, 1999). Furthermore, another study (Junio et al, 2013) suggested that AIPs may be lost rapidly because AIPs were not detected at high-culture densities of around 1 optical density $(\mathrm{OD})_{600}$ *in vitro*, despite a known leaky expression of AIPs prior to agr switch on (Le and Otto, 2015). We further assumed that the timescales of the model variables are slower than that of AIP dynamics even when we explored a ±1 order of magnitude in model parameter values (Supplementary Table S1). We appreciate that this relative timescale is context dependent (eg, the media used in *in vitro* studies and skin conditions) and should be validated through laboratory studies in the future.

Evaluating Equations S6 and S7 at quasi-steady states $\left(dA_I/dt = 0, dE_I/dt = 0\right)$, we obtain the following:

$$A_I(A) = \frac{\left(r_{AI,\min} + r_{AI,\max} \cdot \mathrm{sw}_A\right)}{(\delta_{AI} + \delta_B)} \cdot A = \left(\sigma_{A,\min} + \sigma_{A,\max} \cdot \mathrm{sw}_A(A_I)\right) \cdot A, \tag{S8}$$

$$E_I(E) = \frac{\left(r_{EI,\min} + r_{EI,\max} \cdot \mathrm{sw}_E\right)}{(\delta_{EI} + \delta_B)} \cdot E = \left(\sigma_{E,\min} + \sigma_{E,\max} \cdot \mathrm{sw}_E(E_I)\right) \cdot E, \tag{S9}$$

Where parameters $\sigma_{*,\min} = \frac{r_{*I,\min}}{(\delta_{*I} + \delta_B)}, \sigma_{*,\max} = \frac{r_{*I,\max}}{(\delta_{*I} + \delta_B)}$ represent the ratio of the minimum and maximum synthesis rates and total degradation rates of the AIPs.

The SA and SE QS-switches as functions of the population densities and their crosstalk. Equations S8 and S9 describe the AIP concentrations as a function of their respective species' population densities. Using these, we transform the AIP thresholds $A_{I,\mathrm{th}} = A_I(A_{\mathrm{th}})$ and $E_{I,\mathrm{th}} = E_I(E_{\mathrm{th}})$ of the AIP-induced QS-switches (Equations 4 and 5) to population density thresholds, denoted by A_{th} and E_{th}, as follows:

$$A_{I,\mathrm{th}} = A_I(A_{\mathrm{th}}) = \left(\sigma_{A,\min} + \sigma_{A,\max} \cdot \underbrace{\mathrm{sw}_A\left(A_I = A_{I,\mathrm{th}}\right)}_{=1,\text{from Eq.(4)}}\right) \cdot A_{\mathrm{th}} = \left(\sigma_{A,\min} + \sigma_{A,\max}\right) \cdot A_{\mathrm{th}} = \widehat{A}_{\mathrm{th}}, \tag{S10}$$

$$E_{I,\mathrm{th}} = E_I(E_{\mathrm{th}}) = \left(\sigma_{E,\min} + \sigma_{E,\max} \cdot \underbrace{sw_E\left(E_I = E_{I,th}\right)}_{=1,\text{from Eq.(5)}}\right) \cdot E_{\mathrm{th}} = \left(\sigma_{E,\min} + \sigma_{E,\max}\right) \cdot E_{\mathrm{th}} = \widehat{E}_{\mathrm{th}}, \tag{S11}$$

Using Equations S10 and S11, we can define a model of the QS-switches as a function of bacterial population densities as follows:

$$\mathrm{sw}_A(A) = \begin{cases} 0, & 0 < A < \widehat{A}_{\mathrm{th}}, \\ 1, & A \geq \widehat{A}_{\mathrm{th}}, \end{cases} \tag{S12}$$

$$\mathrm{sw}_E(E) = \begin{cases} 0, & 0 < E < \widehat{E}_{\mathrm{th}}, \\ 1, & E \geq \widehat{E}_{\mathrm{th}}. \end{cases} \tag{S13}$$

In admixtures of SA and SE *in vitro*, the AIPs of SE bind the AIP-sensing module (agrC) of SA and block SA's own AIPs (A_I) from activating its QS-switch, whereas the AIPs of SA do not strongly

inhibit SE from sensing its own AIPs (E_I) (Otto et al, 2001). To model the competitive inhibition of the SA agr switch activation by the AIPs of SE (E_I), we multiply the SA population density–sensing threshold ($\widehat{A}_{\text{th}}$) in Equation S12 by the term ($1+\gamma_{AE}\cdot E_I$) because competitive inhibition is known in enzyme kinetics to effectively increase the sensing threshold without affecting the switch's dynamic range. This gives the following:

$$\text{sw}_A(A) = \begin{cases} 0, & 0 < A < \widehat{A}_{\text{th}}\cdot(1+\gamma_{AE}\cdot E_I), \\ 1, & A \geq \widehat{A}_{\text{th}}\cdot(1+\gamma_{AE}\cdot E_I), \end{cases} \tag{S14}$$

Where the parameter γ_{AE} in Equation S14 represents the strength at which the SE AIPs (E_I) inhibit the activity of the SA QS-switch. The term ($1+\gamma_{AE}\cdot E_I$) of Equation S14 can be approximated as follows:

$$\begin{aligned} 1+\gamma_{AE}\cdot E_I &= 1+\gamma_{AE}\cdot\left(\sigma_{E,\min}+\sigma_{E,\max}\cdot \text{sw}_E(E)\right) \\ &\quad\cdot E \approx 1+\underbrace{\gamma_{AE}\cdot\sigma_{E,\max}}_{=\widehat{\gamma}_{AE}}\cdot \text{sw}_E(E)\cdot E \end{aligned}$$

using Equation S9 and if the value of $\sigma_{E,\min} = \frac{r_{EI,\min}}{\delta_{EI}+\delta_B}$ is much smaller than that of $\sigma_{E,\max} = \frac{r_{EI,\max}}{(\delta_{EI}+\delta_B)}$. This condition holds if $r_{EI,min} \ll r_{EI,max}$, that is, if we can assume that the basal leaky expression rate of SE AIPs ($r_{EI,min}$) is drastically smaller than the maximum expression rate achieved after activating the QS-switch ($r_{EI,max}$). The SA QS-switch in Equation S14 can then be simplified to the following:

$$\text{sw}_A(A) = \begin{cases} 0, & 0 < A < \widehat{A}_{\text{th}}\cdot(1+\widehat{\gamma}_{AE}\cdot\text{sw}_E(E)\cdot E), \\ 1, & A \geq \widehat{A}_{\text{th}}\cdot(1+\widehat{\gamma}_{AE}\cdot\text{sw}_E(E)\cdot E), \end{cases} \tag{S15}$$

Where the parameter $\widehat{\gamma}_{AE}$ represents the strength of the inhibition of each SE cell on the activity of the SA QS-switch.

SE and SA express AMPs and virulence factors through the QS-switch. SE is typically considered a sentinel of the skin (Fournière et al, 2020) because it can actively defend against invading pathogens, such as SA, using several weapons it synthesizes through its inducible QS-switch.

In this study, we consider the synthesis of 2 key SE weapons—AMPs (denoted E_p) and virulence factors (denoted E_{vf})—and model their density-dependent synthesis with ODEs as follows:

$$\frac{dE_p}{dt} = \left(r_{Ep}\cdot \text{sw}_E(E)\right)\cdot E - \left(\delta_{Ep}+\delta_B\right)\cdot E_p, \tag{S16}$$

$$\frac{dE_{\text{vf}}}{dt} = \left(r_{Evf}\cdot \text{sw}_E(E)\right)\cdot E - \left(\delta_{Evf}+\delta_B\right)\cdot E_{\text{vf}}, \tag{S17}$$

Where r_{E^*} denotes the maximum synthesis rates from each SE cell, and δ_{E^*} and δ_B denote the total rate of loss by degradation and skin shedding, respectively. The AMP (E_p) modeled in this study represents the phenol soluble modulins (PSMs) secreted by SE, PSM γ and PSM δ, which specifically kill SA (Cogen et al, 2010). The virulence factor (E_{vf}) in this study represents the skin-damaging protease EcpA, which has been recently discovered to be synthesized through the agr system in a population-dependent manner by some strains of SE isolated from patients with AD (Cau et al, 2021). Many SE strains do not damage the skin, but we model the synthesis of EcpA to ensure that our model can also be used to model the dynamic interplay of SA, the skin, and a skin-damaging SE.

SA is the main colonizing pathogen for patients with AD. To facilitate successful colonization, SA expresses skin barrier–damaging virulence factors such as PSM α and PSM γ through its agr switch (Jenul and Horswill, 2019) and lantibiotics such as aureosins A53 and A70 (dos Santos Nascimento et al, 2005) and Bsa (Daly et al, 2010), which have been shown to kill strains of SE (Daly et al, 2010). We model the syntheses of the SE-killing lantibiotic (denoted as A_p) and skin barrier–damaging virulence factor (denoted as A_{vf}) from SA with ODEs as follows:

$$\frac{dA_p}{dt} = \left(r_{Ap}\cdot \text{sw}_A(A)\right)\cdot A - \left(\delta_{Ap}+\delta_B\right)\cdot A_p, \tag{S18}$$

$$\frac{dA_{\text{vf}}}{dt} = \left(r_{Avf}\cdot \text{sw}_A(A)\right)\cdot A - \left(\delta_{Avf}+\delta_B\right)\cdot A_{\text{vf}}, \tag{S19}$$

Where r_{A^*} denote the maximum synthesis rates from each SA cell, and δ_{A^*} and δ_B denote the total rate of loss by degradation and skin shedding, respectively.

Assumption 6: synthesis of a SE-killing lantibiotic by SA is regulated in a population-dependent manner, which, for simplicity, we assume is through its agr switch. Although it is unclear how the synthesis of SA lantibiotics is regulated, from an evolutionary standpoint, their synthesis is expected to be tightly regulated (Granato et al, 2019) because the production of lantibiotics can be burdensome and reduces cell fitness (Ebner et al, 2018).

Assumption 7: all antimicrobials and virulence factors secreted by SA and SE are unstable, that is, their rate of loss is faster than their synthesis, and so their dynamics is at quasi-steady state. The instability of antimicrobials has been reported as a fundamental roadblock to the manufacture of AMPs from bacteria to address the challenge of antibiotic and multidrug resistance (Mathur et al, 2016; Zhang et al, 2021). Instability (or rapid loss) of virulence factors, such as PSMs secreted from SA, has been suggested because it can be actively degraded by other proteases expressed through the QS-switch system, such as aureolysin (Cheung et al, 2014).

Evaluating Equations S16–19 at steady state, we have the following:

$$A_p(A) = \frac{r_{Ap}}{\delta_{Ap}+\delta_B}\cdot\text{sw}_A(A)\cdot A = \sigma_{Ap}\cdot\text{sw}_A(A)\cdot A, \tag{S20}$$

$$A_{\text{vf}}(A) = \frac{r_{Avf}}{\delta_{Avf}+\delta_B}\cdot\text{sw}_A(A)\cdot A = \sigma_{Avf}\cdot\text{sw}_A(A)\cdot A, \tag{S21}$$

$$E_p(E) = \frac{r_{Ep}}{\delta_{Ep}+\delta_B}\cdot\text{sw}_E(E)\cdot E = \sigma_{Ep}\cdot\text{sw}_E(E)\cdot E, \tag{S22}$$

$$E_{\mathrm{vf}}(E) = \frac{r_{E\mathrm{vf}}}{\delta_{E\mathrm{vf}} + \delta_B} \cdot \mathrm{sw}_E(E) \cdot E \; = \; \sigma_{E\mathrm{vf}} \cdot \mathrm{sw}_E(E) \cdot E, \qquad \text{(S23)}$$

Where $\sigma_{*p} = \frac{r_{*p}}{(\delta_{*p}+\delta_B)}$ and $\sigma_{*\mathrm{vf}} = \frac{r_{*\mathrm{vf}}}{(\delta_{*\mathrm{vf}}+\delta_B)}$ denote the ratios of synthesis (r_{*p},$r_{*\mathrm{vf}}$) and degradation (δ_{*p},$\delta_{*\mathrm{vf}}$,δ_B) rates of the AMPs and virulence factors, respectively. The function $\mathrm{sw}_*(*)$ represents the population density–dependent QS-switches defined in Equations S15 and S13.

SA and SE loss through skin shedding and death by antimicrobials. The cells of both bacterial populations can be lost through skin shedding or killing by the action of the antimicrobial synthesized from the other species. We model these 2 losses in the dynamics of the bacterial populations as follows:

$$\frac{dA}{dt} = \; -\delta_B \cdot A - \delta_{AE} \cdot \frac{E_P}{E_P + E_{P,th}} \cdot A, \qquad \text{(S24)}$$

$$\frac{dE}{dt} = \; -\delta_B \cdot E - \delta_{EA} \cdot \frac{A_P}{A_P + A_{P,th}} \cdot E, \qquad \text{(S25)}$$

Where δ_B denotes the rate of skin shedding, δ_{AE},δ_{EA} denotes the maximum rate of SA-killing by the SE antimicrobial (E_P) and the maximum rate of SE killing by the SA antimicrobial (A_P), respectively, and $E_{P,th}$, $A_{P,th}$ is the concentration of SE and SA antimicrobial, respectively, required to kill one another at half-strength. The second terms of Equations S24 and S25 represent the killing of the bacterial population as a function of the antimicrobial concentration, an equation that appears as follows:

$$\frac{dP}{dt} = \; -\delta \cdot \frac{L}{L + L_{\mathrm{th}}} \cdot P.$$

Where P denotes a bacterial population; L denotes the concentration of an antimicrobial, such as LL-37 (Wei et al, 2021); and L_{th} denotes the threshold concentration of antimicrobial required to kill the bacterial population P at half strength. The solution to this model is as follows:

$$P(t) = P_0 \cdot e^{-\delta \cdot \frac{L}{L+L_{\mathrm{th}}} \cdot t},$$

If we assume that the bacterial population has reached steady state at some fixed time t, the solution (Supplementary Figure S9) depicts a sigmoidal dose–response for the steady state population size of P (y-axis) achieved for (logarithmic) titrations of a fixed concentration of antimicrobial L (x-axis). A similar sigmoidal dose–response was reported in Figure 2 of the study by Wei et al (2021) for the action of AMP LL-37 against SA.

Given that Equations S20 and S22 model the steady state antimicrobial concentrations in terms of the population densities, substituting these into Equations S24 and S25 gives expressions of the death terms in terms of the population densities rather than the antimicrobial concentrations (A_P or E_P):

$$\frac{dA}{dt} = \; -\delta_B \cdot A - \delta_{AE} \cdot \frac{\mathrm{sw}_E(E) \cdot E}{\mathrm{sw}_E(E) \cdot E + \widehat{E}_{p,\mathrm{th}}} \cdot A, \qquad \text{(S26)}$$

$$\frac{dE}{dt} = \; -\delta_B \cdot E - \delta_{EA} \cdot \frac{\mathrm{sw}_A(A) \cdot A}{\mathrm{sw}_A(A) \cdot A + \widehat{A}_{p,\mathrm{th}}} \cdot E. \qquad \text{(S27)}$$

Where $\widehat{E}_{p,\mathrm{th}}$ denotes the SE population required to kill SA, and $\widehat{A}_{p,\mathrm{th}}$ denotes the SA population required to kill SE, both at half-strength.

Assumption 8: antimicrobials synthesized in the skin of patients with AD play an insignificant role to the killing of SA and SE populations.

This is based on the observation that the expression of skin antimicrobials LL-37 and hBD-2 were shown to be deficient at AD lesional sites (Ong et al, 2002), which could in part explain the observed proficiency of SA colonization in patients with AD. Other antimicrobials of the skin are in higher abundance in at least AD lesions than in the skin of healthy controls (Clausen et al, 2018; Harder et al, 2010), but there is little evidence that they reduce SA colonization (Harder et al, 2010).

Damaging of the skin barrier integrity by secreted virulence factors. The virulence factors secreted by SA (A_{vf}) and protease EcpA synthesized by some strains of SE (E_{vf}) damage the skin barrier (Cau et al, 2021; Jenul and Horswill, 2019; Williams et al, 2019). We model the decrease in skin barrier integrity by these factors with the ODE as follows:

$$\frac{dB}{dt} = \; -\delta_{\mathrm{BE}} \cdot E_{\mathrm{vf}} \cdot B - \delta_{\mathrm{BA}} \cdot A_{\mathrm{vf}} \cdot B, \qquad \text{(S28)}$$

Where δ_{BE} and δ_{BA} represent the intensity of the damage caused by the respective virulence factors.

The damaging effect of the PSMs and EcpA secreted by SA and SE, respectively, is caused by their action of cleaving and breaking of the corneodesmosomes and desmosomes that tightly bind corneocytes and keratinocytes to form a physical barrier to bacteria infiltration. When they are broken, the bacteria travel through the gaps created between the skin cells and continue their damaging at increasing depths of the epidermis (Cau et al, 2021; Williams et al, 2019).

From Equation S21 and S23, we have the steady state concentrations of A_{vf} and E_{vf} in terms of the population densities of the respective bacterial species. Substituting these in Equation S28 gives the dynamics of skin barrier integrity in terms of population densities and barrier integrity state as follows:

$$\frac{dB}{dt} = \; -\underbrace{\delta_{BE} \cdot \sigma_{E\mathrm{vf}}}_{=\hat{\delta}_{BE}} \cdot \mathrm{sw}_E \cdot E \cdot B - \underbrace{\delta_{BA} \cdot \sigma_{A\mathrm{vf}}}_{=\hat{\delta}_{BA}} \cdot \mathrm{sw}_A \cdot A \cdot B, \qquad \text{(S29)}$$

This substitution has allowed us to reduce the number of parameters of the system by 2 because 4 parameters are collapsed into 2, as shown in Equation S29.

Determination of model parameters

Derivation of parameters from published data. For skin barrier repair rate (κ_B), we determined $\kappa_B = 0.0711\left(\frac{1}{\text{day}}\right)$ by least-squares fitting of the following model:

$$\frac{dB(t)}{dt} = \kappa_B(1 - B(t)). \tag{S30}$$

We used the time course data of transepidermal water loss of the skin of healthy individuals after exposure to skin-damaging sodium lauryl sulphate (Supplementary Figure S10) extracted from Figure 1a of the study by Hoffman et al (2014) to perform the fitting. We assume that barrier integrity is the inverse of transepidermal water loss and that the skin barrier repair rate of the skin of patients with AD is like that of healthy skin, that is, similar to that of the healthy patients in the study by Hoffman et al (2014). We converted transepidermal water loss measurements $T(t)$ at each time t into a value of the barrier integrity $B(t)$ by $B(t) = \frac{T(t=0)}{T(t)}$.

For the rates of SA and SE loss by skin shedding (δ_B), we determined δ_B=(ln 2)/24 = 0.0289 ([1/day]), because the half-life of epidermis cells is about 24 days (Koster, 2009).

For population density thresholds at which the QS agr-switches of SE and SA are activated ($\widehat{E}_{th}$ *and* $\widehat{A}_{th}$), we determined $\widehat{E}_{\text{th}} = 1.13 \times 10^8$ ([colony − forming unit / cm^2]) by converting the population density of SE at half-activation of its QS agr switch ($\widehat{E}_{\text{th}} = 1.424$ [OD$_{600}$]) when the expression of the agr promoter reaches half its maximum (black dashed lines in Supplementary Figure S11) from *in vitro* data in Figure 2 of the study by Olson et al (2014).

To obtain the value of the population density in units of colony-forming unit (CFU)/cm^2, we first convert the value in units of OD to that in CFU/ml and then to CFU/cm^2.

To convert OD to CFU/ml, we use the data of Hinds and Peterson (1963) and conduct least-square fitting to an assumed linear relationship between colony counts (CFU/ml) and OD of *Staphylococci* suspension (Supplementary Figure S12), similarly to that in Yap and Trau (2019), to obtain the following formulae:

$$X[\text{OD}] = 0.0218 \cdot 10^{-7}[\text{OD}\cdot\text{mL/CFU}]\cdot C\left[10^7\ \text{CFU/mL}\right] + 0.0569[\text{OD}], \tag{S31}$$

Where X represents the measured OD of the culture population in units of OD, and C represents the *Staphylococci* population density in units of 10^7 CFU/ml. We assume that the differences in wavelengths used to measure OD (OD$_{650}$ in the study by Hinds and Peterson [1963] and OD$_{600}$ in the study by Olson et al [2014]) will not change the order of magnitudes of our estimates in CFU/ml. From Equation S31, we obtain the following:

$$1.424\ [\text{OD}] = 0.0218\cdot 10^{-7}[\text{OD}\cdot\text{mL/CFU}]\cdot(\widehat{E}_{\text{th}}[\text{CFU/mL}]) + 0.0569\ [\text{OD}], \Rightarrow \widehat{E}_{\text{th}} = 62.7 \times 10^7[\text{CFU/mL}].$$

It is further converted to the following:

$$\widehat{E}_{\text{th}}\left[\text{CFU/cm}^2\right] = \left(62.7 \times 10^7[\text{CFU/ml}]\right)\cdot\frac{0.9[\text{ml}]}{5[\text{cm}^2]} = 1.13 \times 10^8\left[\text{CFU/cm}^2\right],$$

using the following formula:

$$x\left[\text{CFU}\,/\,\text{cm}^2\right] = \frac{\text{number of colonies (CFU)} \times \text{volume of homogenate (mL)} \times \text{dilution factor}}{\text{volume of sample plated (ml)} \times \text{area sampled (cm}^2\text{)}} = x[\text{CFU}\,/\,\text{ml}]\cdot\frac{\text{volume of homogenate (ml)}}{\text{area sampled (cm}^2\text{)}}, \tag{S32}$$

Where volume of homogenate = 0.9 ml, and area swabbed =5 cm^2, is taken from the study by Cau et al (2021) who quantified the density of SA and SE from skin swabs of a 5 cm^2 area and inoculated in a media of volume 0.9 ml.

We assume that the threshold population density for activating the SA QS agr-switch ($\widehat{A}_{\text{th}}$) is of a similar magnitude to $\widehat{E}_{\text{th}}$ and define the nominal value of $\widehat{A}_{\text{th}} = \widehat{E}_{\text{th}}$.

We obtained the nominal values of the SA and SE growth rates (κ_A,κ_E) = (17.9, 17.0)[1/day] and population carrying capacities $A_{max} = E_{max} = 1.11\times10^9$[CFU/cm^2] by least-squares fitting of the logistic growth equations as follows:

$$\frac{\text{d}A(t)}{\text{dt}} = \kappa_A A(t)\left(1 - \frac{A(t)}{A_{\text{max}}}\right), \tag{S33}$$

$$\frac{dE(t)}{dt} = \kappa_E E(t)\left(1 - \frac{E(t)}{E_{\text{max}}}\right). \tag{S34}$$

We used *in vitro* time-course growth data of monocultures of SA and SE from 4 sources (James et al, 2013; Miajlovic et al, 2010; Olson et al, 2014; Toribio et al, 2018) (Supplementary Figure S13) to perform the fitting. Equations S33 and S34 were obtained from our model equations (Equations 1 and 2) by setting $B(t)$=0 (no skin barrier involved) and $\delta_A = \delta_E = 0$ (no skin turnover) and ignoring any effect either species has on the other because data are of

monocultures in the absence of skin. The fitting of the model to the data from each source is shown in Supplementary Figure S13, and the optimal parameter values estimated are summarized in Supplementary Table S2.

We take an average of the 4 estimated κ_A values (26.2, 23.3, 12.4, and 9.75 [1/day]) to obtain a nominal value of κ_A=17.9 [1/day] and the average of the 3 estimated κ_E values (16.2, 21.4 and 13.5 [1/day]) to obtain a nominal value of κ_E=17.0 [1/day]. However, given the variation in the growth rates (from different nutrient conditions and strains), we explore the values of κ_A and κ_E in the range of [9, 27] [1/day], defined by rounding down the minimum and rounding up the maximum of all the growth rate estimates from all fits of both species, as reported in Supplementary Table S2.

We assume that SA and SE have the same carrying capacity (A_{max}=E_{max}) when grown in *in vitro* monocultures owing to the abundance of nutrients for growth and that the maximum of the estimated carrying capacity (13.5 [OD] from Supplementary Table S2) is the absolute maximum carrying capacity on the skin because these monocultures are grown in much richer nutrient conditions *in vitro* than would be found on skin.

Using Equations S31 and S32, we convert the carrying capacity of SA (A_{max}) from units of OD to units of CFU/cm^2 and obtain the following:

$$\begin{aligned} A_{\max}\,[\mathrm{CFU/ml}] &= \frac{(13.5\ -0.0569)\,[\mathrm{OD}]}{0.0218\cdot 10^{-7}(\mathrm{OD\cdot ml/CFU})} \\ &= 617\times 10^{7}[\mathrm{CFU/ml}], \end{aligned}$$

and

$$\begin{aligned} A_{\max}\left[\mathrm{CFU/cm^2}\right] &= \left(617\left[10^{7}\mathrm{CFU/ml}\right]\right)\cdot\frac{0.9\ \mathrm{ml}}{5\ \mathrm{cm^2}} \\ &= 1.11\times 10^{9}\left[\mathrm{CFU/cm^2}\right]. \end{aligned}$$

We define the nominal value of E_{max}=A_{max}.

For the strength at which SE inhibits the activation of the SA QS agr switch ($\widehat{\gamma}_{AE}$), we obtained $\widehat{\gamma}_{AE} = 1.06\times 10^{-8}$ [cm^2/CFU] by deriving the ratio of SA agr expression levels when SA is grown in a media containing accumulations of SE AIP (A_{agr_epi}) (ie, the supernatant of the media in which SE was grown to high enough densities to have expressed its agr and synthesized AIPs) versus grown in media without SE AIP ($A_{agr\_no\_epi}$) using the data from Figure 2c of the study by Williams et al (2019) (Supplementary Table S3). Figure 2c of the study by Williams et al (2019) describes the agr (I) expression of SA USA300 grown with 25% supernatant from overnight cultures (10 [OD600$_{nm}$]) of SE agr types I (RP62A) wild-type strain and an AIP-knockout (Δ AIP) strain, relative to a control of SA grown in fresh media.

From the definition of the SA QS-agr switch in Equation S15, namely,

$$\mathrm{sw}_A(A) = \begin{cases} 0, & 0 < A < \widehat{A}_{\mathrm{th}}\cdot(1+\widehat{\gamma}_{AE}\cdot \mathrm{sw}_E(E)\cdot E), \\ 1, & A \geq \widehat{A}_{\mathrm{th}}\cdot(1+\widehat{\gamma}_{AE}\cdot \mathrm{sw}_E(E)\cdot E), \end{cases}$$

When the SA QS agr-switch is on ($\mathrm{sw}_A(A)$=1), the SA agr expression level (A_{agr}) satisfies the following:

$$\frac{A}{1+\widehat{\gamma}_{AE}\cdot \mathrm{sw}_E(E)\cdot E} = A_{\mathrm{agr}} \geq \widehat{A}_{\mathrm{th}}.$$

Therefore, the ratio of the SA agr expression grown in the supernatant of a SE that expressed AIPs ($*_{epi}$) versus that grown in the supernatant of a mutant SE that cannot express AIPs ($*_{no\_epi}$) is given by the following:

$$\begin{aligned} \frac{A_{\mathrm{agr\_epi}}(t)}{A_{\mathrm{agr\_no\_epi}}(t)} &= \frac{A_{\mathrm{epi}}(t)}{1+\widehat{\gamma}_{\mathrm{AE}}\cdot \mathrm{sw}_{\mathrm{E}}\left(E_{\mathrm{epi}}\right)\cdot E_{\mathrm{epi}}(t)} \\ &\quad\cdot\frac{1+\widehat{\gamma}_{\mathrm{AE}}\cdot \mathrm{sw}_{\mathrm{E}}\left(E_{\mathrm{no\_epi}}\right)\cdot E_{\mathrm{no\_epi}}(t)}{A_{\mathrm{no\_epi}}(t)}. \end{aligned} \quad \text{(S35)}$$

We can simplify Equation S35 as follows:

$$\begin{aligned} \frac{A_{\mathrm{agr\_epi}}(t)}{A_{\mathrm{agr\_no\_epi}}(t)} &= \frac{A_{\mathrm{epi}}(t)}{1+\widehat{\gamma}_{\mathrm{AE}}\cdot \mathrm{sw}_{\mathrm{E}}\left(E_{\mathrm{epi}}\right)\cdot E_{\mathrm{epi}}(t)} \\ &\quad\cdot\frac{1+\widehat{\gamma}_{\mathrm{AE}}\cdot \mathrm{sw}_{\mathrm{E}}\left(E_{\mathrm{no\_epi}}\right)\cdot E_{\mathrm{no\_epi}}(t)}{A_{\mathrm{no\_epi}}(t)} \\ &= \frac{A_{\mathrm{epi}}(t)}{1+\widehat{\gamma}_{\mathrm{AE}}\cdot \mathrm{sw}_{\mathrm{E}}\left(E_{\mathrm{epi}}\right)\cdot E_{\mathrm{epi}}(t)}\cdot\frac{1}{A_{\mathrm{no\_epi}}(t)} \\ &= \frac{A_{\mathrm{epi}}(t)}{1+\widehat{\gamma}_{\mathrm{AE}}\cdot \widehat{E}}\cdot\frac{1}{A_{\mathrm{no\_epi}}(t)} = \frac{1}{1+\widehat{\gamma}_{\mathrm{AE}}\cdot \widehat{E}} \end{aligned}$$

through 3 assumptions:

- $\mathrm{sw}_{\mathrm{E}}(E_{\mathrm{no\_epi}}) = 0$ because the SE agr switch cannot be activated without SE AIPs.
- $\mathrm{sw}_{\mathrm{E}}(E_{\mathrm{epi}})$=1 when $E_{\mathrm{epi}}(t) = \widehat{E}$, that is, that the agr switch is activated when the SE population reaches a maximum ($\widehat{E}$).
- $A_{\mathrm{epi}}(t) = A_{\mathrm{no\_epi}}(t)$ because SE AIPs do not affect the growth of SA (Williams et al, 2019).

Williams et al (2019) reported an overnight bacterial density of approximately 10 [OD$_{600nm}$] for all *Staphylococci* (SA and coagulase negative staphylococci). Using Equations S31 and S32, we convert the maximum population size of SE in this study ($\widehat{E}$) from units of OD to units of CFU/cm^2, and obtain the following:

$$\begin{aligned} \widehat{E}\,[\mathrm{CFU/ml}] &= \frac{(10\ -0.0569)\,[\mathrm{OD}]}{0.0218\cdot 10^{-7}(\mathrm{OD\cdot mL/CFU})} \\ &= 456\times 10^{7}[\mathrm{CFU/ml}], \end{aligned}$$

and

$$\widehat{E}\left[\mathrm{CFU/cm^2}\right] = \left(456\left[10^7\mathrm{CFU/ml}\right]\right)\cdot\frac{0.9\ \mathrm{ml}}{5\ \mathrm{cm^2}} = 8.21\times10^8\left[\mathrm{CFU/cm^2}\right].$$

We obtain the following:

$$\widehat{\gamma}_{AE} = \frac{1}{\widehat{E}}\cdot\left(\frac{A_{agr\_no\_epi}(t)}{A_{agr\_epi}(t)}-1\right) = \frac{1}{8.21\times10^8\left[\frac{\mathrm{CFU}}{\mathrm{cm^2}}\right]}\cdot\left(\frac{128\ [\%\ \mathrm{RFU\ to\ control}]}{11.0\ [\%\ \mathrm{RFU\ to\ control}]}-1\right) = 1.30\times10^{-8}\left[\frac{\mathrm{cm^2}}{\mathrm{CFU}}\right],$$

using $A_{agr\_no\_epi}(t) = 128$ [% RFU to control], $A_{agr\_epi}(t) = 11.0$ [% RFU to control] from SA agr (I) activity (Supplementary Table S3), and $\widehat{E} = 8.21\times10^8\ \left[\frac{\mathrm{CFU}}{\mathrm{cm^2}}\right]$.

Motivation for how the remaining parameter values were chosen. For the rate of barrier damage by SA and SE virulence factors ($\widehat{\delta}_{BA}$ and $\widehat{\delta}_{BE}$), some strains of SA and SE damage the skin barrier integrity by secreting the virulence factors and proteases that cleave corneodesmosomes and demosomes (Cau et al, 2021; Williams et al, 2019). As far as we are aware, there are no time-course data from which to estimate the specific rate of barrier damage by SA ($\widehat{\delta}_{BA}$). We therefore set an arbitrary value of $\widehat{\delta}_{BA} = 1\times10^{-9}$ [$\mathrm{cm^2}$/(CFU × day)] to reflect the magnitudes of the other estimated parameter value in [$\mathrm{cm^2}$/CFU] and vary the value of $\widehat{\delta}_{BA}$ by 2 orders of magnitude to investigate how the system is affected. We assume that SE can be both skin damaging and non-damaging. Studies have found no significant correlation between SE populations and AD severity scores (Byrd et al, 2017); however, certain SE strains isolated from patients with AD have been found to be as damaging as SA (Cau et al, 2021). In accordance with literature, we sample the rate of skin barrier damage by SE ($\widehat{\delta}_{BE}$) over 4 orders of magnitude (1×10^{-12}, 1×10^{-8} [$\mathrm{cm^2}$/[CFU × day]) and set $\widehat{\delta}_{BE} = 0$ when $\widehat{\delta}_{BE} < 1\times10^{-10}$ ($\mathrm{cm^2}$/[CFU × day]) (ie, the minimum rate of damage by SA).

For population size of SA and SE required to kill the opposite microbe at half-strength ($\widehat{A}_{p,th}$ and $\widehat{E}_{p,th}$), we assume that their parameter values $\widehat{A}_{p,th}$, $\widehat{E}_{p,th}$ are the same as the parameters representing the threshold population sizes that activate the QS agr switch ($\widehat{A}_{th}$, $\widehat{E}_{th}$) because the agr of SA must switch on to produce the antimicrobials that enact the killing of SE and vice versa. Because the values of ($\widehat{A}_{p,th}$, $\widehat{E}_{p,th}$) are unknown, we vary their values by 2 orders of magnitude from their nominal values to investigate the effect on the system behavior.

For the rate of SE killing by SA (δ_{EA}) and vice versa (δ_{AE}), we estimate the rate of SA-killing by SE (δ_{AE}) using *in vitro* data of the relative drop in SA population after its culture in spent supernatants in which SE was grown to high densities overnight (Nakatsuji et al, 2017) extracted from Supplementary Figure S8a of the study by Nakatsuji et al (2017) (Supplementary Figure S14). Because the data are of *in vitro* measurements in the absence of skin barrier ($B(t) = 0$) and loss by skin shedding ($\delta_B = 0$), we fit the data to a modified version of Equation S26 as follows:

$$\frac{dA}{dt} = \kappa_A A(t)\left(1-\frac{A(t)}{A_{max}}\right) - \delta_{AE}\cdot\frac{sw_E(E)\cdot E}{sw_E(E)\cdot E+\widehat{E}_{p,th}}\cdot A = \kappa_A A(t)\left(1-\frac{A(t)}{A_{max}}\right) - \delta_{AE}\cdot\frac{E_{max}}{E_{max}+\widehat{E}_{p,th}}\cdot A, \quad \text{(S36)}$$

where we assume that SE population is at its maximum $E = E_{max}$ as shown by the open squares in Supplementary Figure S11 at 11 hours onward, and thus its QS-switch is on ($sw_E(E_{max}) = 1$). This is because SA is cultured in the spent supernatant of a SE population that has been grown overnight. Fitting of the data (Supplementary Figure S14) to the model with the nominal values of κ_A=17.9 [1/day], $A_{max} = 1.11\times10^9$[CFU/$\mathrm{cm^2}$], $E_{max} = 1.11\times10^9$[CFU/$\mathrm{cm^2}$] and $\widehat{E}_{p,th} = 1.13\times10^8$[CFU/$\mathrm{cm^2}$] $\widehat{A}_{p,th}$ $\widehat{E}_{p,th}$, we estimated δ_{AE}=478 [1/day].

To the best of our knowledge, we cannot estimate the death rate of SE from killing by SA (δ_{EA} from Equation 29) owing to the lack of data. For simplicity, we assume that $\delta_{EA} = \delta_{AE} = 478$ [1/day]. We set the nominal values of δ_{AE} and δ_{EA} as the upper bound of the range because the killing capacity of SE on skin is unlikely to be as large compared with an *in vitro* setting where SE is grown to a maximum population size overnight. The population sizes of SA and SE on the skin should be smaller than that in *in vitro* cultures because the human skin is less nutrient rich than *in vitro* cultures. Owing to the uncertainties in these parameters, we vary δ_{EA} and δ_{AE} by 2 orders of magnitude to investigate how it impacts the system behavior.

For barrier-mediated inhibition of SA and SE growth (γ_{AB} and γ_{EB}), we took an analytical approach to choose a biologically relevant parameter range.

Let (A^*, E^*, B^*) denote the steady state. Evaluating $\frac{dB}{dt}$ (Equation 3 + Equation S29) at the steady state gives the following:

$$0 = \kappa_B \cdot (1 - B^*) - \widehat{\delta}_{BE} \cdot sw_E(E^*) \cdot E^* \cdot B^* - \widehat{\delta}_{BA} \cdot sw_A(A^*) \cdot A^* \cdot B^*$$

$$\Rightarrow B^* = \frac{\kappa_B}{\kappa_B + \widehat{\delta}_{BE} \cdot sw_E(E^*) \cdot E^* + \widehat{\delta}_{BA} \cdot sw_A(A^*) \cdot A^*}$$

If $\widehat{\delta}_{BE}, \widehat{\delta}_{BA} \neq 0$, SA and SE QS-switches must be off ($sw_A(A^*)=0$ and $sw_E(E^*)=0$) to achieve $B^*=1$ with non-zero steady state population densities ($A^*, E^* \neq 0$). The corresponding steady states (A^*, E^*) are obtained by evaluating $\frac{dA}{dt}$ (Equation 1 + Equation S24) and $\frac{dE}{dt}$ (Equation 2 + Equation S25) at $B^*=1$, $sw_A(A^*)=0$, and $sw_E(E^*)=0$, as follows:

$$0 = \frac{\kappa_A}{1+\gamma_{AB}}\left(1 - \frac{A^*}{A_{max}}\right)A^* - \delta_B \cdot A^* \Rightarrow A^* = A_{max}\left(1 - \frac{\delta_B \cdot (1+\gamma_{AB})}{\kappa_A}\right)$$

and

$$0 = \frac{\kappa_E}{1+\gamma_{EB}}\left(1 - \frac{E^*}{E_{max}}\right)E^* - \delta_B \cdot E^* \Rightarrow E^* = E_{max}\left(1 - \frac{\delta_B \cdot (1+\gamma_{EB})}{\kappa_E}\right).$$

Therefore,

$$\gamma_{AB} = \frac{\kappa_A}{\delta_B}\left(1 - \frac{A^*}{A_{max}}\right) - 1 \quad \text{(S37)}$$

$$\gamma_{EB} = \frac{\kappa_E}{\delta_B}\left(1 - \frac{E^*}{E_{max}}\right) - 1 \quad \text{(S38)}$$

As stated earlier, because the QS-switches are off, the populations of SA and SE are less than their respective switch thresholds $\widehat{A}_{th}$ and $\widehat{E}_{th}$, by the definition of the switch models in Equations S12 and S13. Therefore, the steady state population densities must also be less than the switch thresholds, namely,

$$0 \leq A^* < \widehat{A}_{th}, \quad \text{(S39)}$$

$$0 \leq E^* < \widehat{E}_{th}. \quad \text{(S40)}$$

Where $\widehat{A}_{th} = 1.13 \times 10^8$, and $\widehat{E}_{th} = 1.13 \times 10^8$ [CFU/cm^2] (section on population density thresholds at which the QS agr-switches of SE and SA are activated [$\widehat{E}_{th}$ and $\widehat{A}_{th}$]).

Using Equation S39 and S40, we can determine the ranges of γ_{AB} and γ_{EB} (no units) for the existence of $B^*=1$ by substituting A^* and E^* at their boundaries with our nominal values of κ_A=17.9 [1/day], κ_E=17.0 [1/day],-A_{max}=1.11×10^9[CFU/cm^2], E_{max}=1.11×10^9[CFU/cm^2], and δ_B=0.0289 [1/day], into Equations S37 and S38 to obtain the following:

$$555 < \gamma_{AB} < 618,$$
$$528 < \gamma_{EB} < 587.$$

We chose nominal values of $\gamma_{AB} = 587$ and $\gamma_{EB} = 558$ in our simulations and vary the parameter values by 2 orders of magnitude to investigate how this affects the system behaviours.

Mathematical analysis of steady states

Method overview. We generated 10^6 virtual skin sites by randomly sampling values of 15 of 17 model parameters from a log-uniform distribution with ranges defined in Supplementary Table S1. We kept 2 parameter values fixed, the maximum capacities of SA (A_{max}) and SE (E_{max}), because these parameters should not influence the types of virtual skin sites observed. We then analyzed their steady states to evaluate the variety of virtual skin types we could observe from our model. Our model equations suggest 9 possible regions for steady states to be found in, depending on whether the QS-switches are active or inactive (Supplementary Figure S15).

Steady state analysis when SA and SE QS-switches are inactive. When both SA and SE QS are inactive ($sw_E(E) = sw_A(A) = 0$), steady states for SA, SE, and barrier integrity (A^*, E^*, B^*) are computed as follows:

$$\frac{dA}{dt} = \frac{\kappa_A \cdot A}{1+\gamma_{AB} \cdot B}\left(1 - \frac{A}{A_{max}}\right) - \delta_B \cdot A = 0, \Rightarrow A^* = A_{max}\left(1 - \frac{\delta_B \cdot (1+\gamma_{AB})}{\kappa_A}\right) \quad \text{(S41)}$$

$$\frac{dE}{dt} = \frac{\kappa_E \cdot E}{1+\gamma_{EB} \cdot B}\left(1 - \frac{E}{E_{max}}\right) - \delta_B \cdot E = 0 \Rightarrow E^* = E_{max}\left(1 - \frac{\delta_B \cdot (1+\gamma_{EB})}{\kappa_E}\right) \quad \text{(S42)}$$

$$\frac{dB}{dt} = \kappa_B \cdot (1 - B) = 0, \Rightarrow B^* = 1 \quad \text{(S43)}$$

Because the QS-switches are inactive, the populations of SA and SE must be less than their respective switch thresholds $\widehat{A}_{\text{th}}$ and $\widehat{E}_{\text{th}}$, that is, $0 \le A^* < \widehat{A}_{\text{th}}$ and $0 \le E^* < \widehat{E}_{\text{th}}$.

When both QS-switches are inactive, there are 4 possible steady states on the basis of Equations S41–43, depending on whether SA or SE populations densities are zero or non-zero:

$(A_1^*, E_1^*, B_1^*) = (0, 0, 1)$,
corresponding to region 1 in Supplementary Figure S15

$(A_2^*, E_2^*, B_2^*) = (A_2^* > 0, 0, 1)$,
corresponding to region 2 in Supplementary Figure S15

$(A_3^*, E_3^*, B_3^*) = (0, E_3^* > 0, 1)$,
corresponding to region 3 in Supplementary Figure S15

$(A_4^*, E_4^*, B_4^*) = (A_4^* > 0, E_4^* > 0, 1)$,
corresponding to region 4 in Supplementary Figure S15

We substitute each steady state into the following Jacobian matrix to check its stability. If the real part of all eigenvalues is negative, the steady state is stable, as follows:

$$J_1 = \begin{bmatrix} -\delta_B - \left(\frac{\kappa_A}{1+\gamma_{AB}\cdot B^*}\cdot\left(\frac{A^*}{A_{max}} - 1\right) - \left(\frac{A^*\kappa_A}{A_{max}(1+\gamma_{AB}\cdot B^*)}\right)\right) & 0 & \frac{A^*\cdot\gamma_{AB}\cdot\kappa_A}{(1+\gamma_{AB}\cdot B^*+1)^2}\cdot\left(\left(\frac{A^*}{A_{max}} - 1\right)\right) \\ 0 & -\delta_B - \left(\frac{\kappa_E}{1+\gamma_{EB}\cdot B^*}\cdot\left(\frac{E^*}{E_{max}} - 1\right) - \left(\frac{E^*\kappa_E}{E_{max}(1+\gamma_{AB}\cdot B^*)}\right)\right) & \frac{E^*\cdot\gamma_{EB}\cdot\kappa_E}{(1+\gamma_{EB}\cdot B^*+1)^2}\cdot\left(\left(\frac{E^*}{E_{max}} - 1\right)\right) \\ 0 & 0 & -\kappa_B \end{bmatrix}$$

Steady states when only SE QS-switch is active. When SE QS is active ($sw_E(E) = 1$) and SA QS is inactive ($sw_A(A) = 0$), the steady states for SA, SE, and barrier integrity (A^*, E^*, B^*) are computed as follows:

$$\frac{dA}{dt} = \frac{\kappa_A\cdot A}{1+\gamma_{AB}\cdot B}\left(1-\frac{A}{A_{max}}\right) - \delta_{AE}\cdot\frac{sw_E(E)\cdot E}{sw_A(E)\cdot E + \widehat{E}_{p,th}} - \delta_B\cdot A = 0$$

$$\Rightarrow A^* = A_{max}\cdot\left(1-\left(\frac{1+\gamma_{AB}\cdot B^*}{\kappa_A}\right)\cdot\left(\delta_B + \delta_{AE}\cdot\frac{sw_E(E)\cdot E^*}{sw_A(E)\cdot E^* + \widehat{E}_{p,th}}\right)\right) \quad \text{(S44)}$$

$$\frac{dE}{dt} = \frac{\kappa_E\cdot E}{1+\gamma_{EB}\cdot B}\left(1-\frac{E}{E_{max}}\right) - \delta_B\cdot E = 0$$

$$\Rightarrow E^* = E_{max}\left(1-\frac{\delta_B\cdot(1+\gamma_{EB}\cdot B^*)}{\kappa_E}\right) \quad \text{(S45)}$$

$$\frac{dB}{dt} = \kappa_B\cdot(1-B) - \widehat{\delta}_{BE}\cdot sw_E(E)\cdot E\cdot B = 0$$

$$\Rightarrow B^* = \frac{\kappa_B}{\kappa_B + \widehat{\delta}_{BE}\cdot sw_E(E^*)\cdot E^*} \quad \text{(S46)}$$

If $\widehat{\delta}_{BE} = 0$, steady state barrier integrity $B^* = 1$.

Substituting Equation S46 into Equation S45 results in the following quadratic:

$$\kappa_E\cdot\delta_{EA}\cdot E^{*2} + (\kappa_E\cdot\kappa_B + E_{max}\cdot\delta_B\cdot\widehat{\delta}_{BE} - E_{max}\cdot\kappa_E\cdot\widehat{\delta}_{BE})\cdot E^* + E_{max}(\delta_B\cdot\kappa_B + \delta_B\cdot\gamma_{EB}\cdot\kappa_B - \kappa_E\cdot\kappa_B) = 0$$

On the basis of Descartes' rule of signs, we know that there can be between zero to 2 positive real roots of E^* depending on the parameter values in the system. We computed the 2 solutions for E^* using the symbolic toolbox in MATLAB and then calculated the corresponding values for A^* and B^*, for each value of E^*, by respectively substituting into Equation S44 and Equation S46.

Because only the SE QS-switch is on, the population of SE must be greater than its QS-switch threshold $\widehat{E}_{\text{th}}$, whereas SA must be smaller than its QS-switch threshold $\widehat{A}_{\text{th}}$:

$$\widehat{E}_{\text{th}} \le E^* \le E_{max},$$

$$0 \le A^* < \widehat{A}_{\text{th}}.$$

There are 4 possible solutions for when only SE QS-switch is active, where SA population density may be zero or non-zero:

$(A_{5m}^*, E_{5m}^*, B_{5m}^*) = (0, \widehat{E}_{\text{th}} \le E_{5m}^* \le E_{max}, B_{5m}^*)$,
corresponding to region 5 in Supplementary Figure S15

$(A_{5n}^*, E_{5n}^*, B_{5n}^*) = (0, \widehat{E}_{\text{th}} \le E_{5n}^* \le E_{max}, B_{5n}^*)$,
corresponding to region 5 in Supplementary Figure S15

$(A_{6m}^*, E_{6m}^*, B_{6m}^*) = (0 < A_{6m}^* < \widehat{A}_{\text{th}}, \widehat{E}_{\text{th}} \le E_{6m}^* \le E_{max}, B_{6m}^*)$,
corresponding to region 6 in Supplementary Figure S15

$(A_{6n}^*, E_{6n}^*, B_{6n}^*) = (0 < A_{6n}^* < \widehat{A}_{\text{th}}, \widehat{E}_{\text{th}} \le E_{6n}^* \le E_{max}, B_{6n}^*)$,
corresponding to region 6 in Supplementary Figure S15

Where $E_{5m}^* = E_{6m}^*$, $E_{5n}^* = E_{6n}^*$, $B_{5m}^* = B_{6m}^*$, and $B_{5n}^* = B_{6n}^*$.

We analyze the stability of these steady states using the following Jacobian matrix:

Steady states when only SA QS-switch is active. When SA QS is active ($sw_A(A)=1$) and SE QS is inactive ($sw_E(E)=0$), the steady states SA, SE, and barrier integrity (A^*, E^*, B^*) are computed as follows:

$$J_2 = \begin{bmatrix} -\delta_B - \left(\frac{\kappa_A}{1+\gamma_{AB}\cdot B^*}\cdot\left(\frac{A^*}{A_{max}}-1\right)\right) - \frac{E^*\cdot\hat{\delta}_{AE}}{E^*+\hat{E}_{p,th}} - \left(\frac{A^*\kappa_A}{A_{max}(1+\gamma_{AB}\cdot B^*)}\right) & -A^*\cdot\left(\frac{\hat{\delta}_{AE}}{(E^*+\hat{E}_{p,th})} - \frac{E^*\cdot\hat{\delta}_{AE}}{(E^*+\hat{E}_{p,th})^2}\right) & \frac{A^*\cdot\gamma_{AB}\cdot\kappa_A}{(1+\gamma_{AB}\cdot B^*+1)^2}\cdot\left(\left(\frac{A^*}{A_{max}}-1\right)\right) \\ 0 & -\delta_B - \left(\frac{\kappa_E}{1+\gamma_{EB}\cdot B^*}\cdot\left(\frac{E^*}{E_{max}}-1\right) - \left(\frac{E^*\kappa_E}{E_{max}(1+\gamma_{AB}\cdot B^*)}\right)\right) & \frac{E^*\cdot\gamma_{EB}\cdot\kappa_A}{(1+\gamma_{EB}\cdot B^*+1)^2}\cdot\left(\left(\frac{E^*}{E_{max}}-1\right)\right) \\ 0 & -B^*\cdot\hat{\delta}_{BE} & -\kappa_B - E^*\cdot\hat{\delta}_{BE} \end{bmatrix}$$

$$\begin{aligned} \frac{dA}{dt} &= \frac{\kappa_A\cdot A}{1+\gamma_{AB}\cdot B}\left(1-\frac{A}{A_{max}}\right) - \delta_B\cdot A = 0 \\ \Rightarrow A^* &= A_{max}\left(1-\frac{\delta_B\cdot(1+\gamma_{AB}\cdot B^*)}{\kappa_A}\right) \end{aligned} \tag{S47}$$

$$\begin{aligned} &\frac{dE}{dt} = \frac{\kappa_E\cdot E}{1+\gamma_{EB}\cdot B}\left(1-\frac{E}{E_{max}}\right) - \delta_{EA}\cdot\frac{sw_A(A)\cdot A}{sw_A(A)\cdot A+\hat{A}_{p,th}}\cdot E - \delta_B\cdot E = 0 \\ &\Rightarrow E^* = E_{max}\cdot\left(1-\left(\frac{1+\gamma_{EB}\cdot B^*}{\kappa_E}\right)\cdot\left(\delta_B+\delta_{EA}\cdot\frac{sw_A(A)\cdot A^*}{sw_A(A)\cdot A^*+\hat{A}_{p,th}}\right)\right) \end{aligned} \tag{S48}$$

$$\begin{aligned} \frac{dB}{dt} &= \kappa_B\cdot(1-B) - \hat{\delta}_{BA}\cdot sw_A(A)\cdot A\cdot B = 0 \\ \Rightarrow B^* &= \frac{\kappa_B}{\kappa_B+\hat{\delta}_{BA}\cdot sw_A(A^*)\cdot A^*}. \end{aligned} \tag{S49}$$

Substituting Equation S49 into Equation S47 results in a quadratic equation for A^*:

$$\begin{aligned} &\kappa_A\cdot\hat{\delta}_{BA}\cdot A^{*2} + (\kappa_A\cdot\kappa_B + A_{max}\cdot\delta_B\cdot\hat{\delta}_{BA} - A_{max}\cdot\kappa_A\cdot\hat{\delta}_{BA})\cdot A^* \\ &+A_{max}(\delta_B\cdot\kappa_B + \delta_B\cdot\gamma_{AB}\cdot\kappa_B - \kappa_A\cdot\kappa_B) = 0 \end{aligned}$$

On the basis of Descartes' rule of signs, we know that there can be between zero to 2 positive real roots of A^* depending on the parameter values in the system. We compute the 2 solutions for A^* using the symbolic toolbox in MATLAB and then calculate the respective values of E^* and B^* by substituting each value of A^* into Equation S48 and Equation S49.

Because only the SA QS-switch is active, the population of SA must be greater than its QS-switch threshold $\hat{A}_{th}$, whereas SE must be smaller than its a QS-switch threshold $\hat{E}_{th}$:

$$\hat{A}_{th} \le A^* \le A_{max},$$

$$0 \le E^* < \hat{E}_{th}.$$

Again, there are 4 possible solutions for when only SA QS-switch is active depending on whether SE population sizes are zero or non-zero:

$(A^*_{7m}, E^*_{7m}, B^*_{7m}) = (\hat{A}_{th} \le A^*_{7m} \le A_{max}, 0, B^*_{7m})$,
corresponding to region 7 in Supplementary Figure S15
$(A^*_{7n}, E^*_{7n}, B^*_{7n}) = (\hat{A}_{th} \le A^*_{7n} \le A_{max}, 0, B^*_{7n})$,
corresponding to region 7 in Supplementary Figure S15
$(A^*_{8m}, E^*_{8m}, B^*_{8m}) = (\hat{A}_{th} \le A^*_{8m} \le A_{max}, 0 < E^*_{8m} < \hat{E}_{th}, B^*_{8m})$,
corresponding to region 8 in Supplementary Figure S15
$(A^*_{8n}, E^*_{8n}, B^*_{8n}) = (\hat{A}_{th} \le A^*_{8n} \le A_{max}, 0 < E^*_{8n} < \hat{E}_{th}, B^*_{8n})$,
corresponding to region 8 in Supplementary Figure S15
where $A^*_{7m} = A^*_{8m}$, $A^*_{7n} = A^*_{8n}$, $B^*_{7m} = B^*_{8m}$, and $B^*_{7n} = B^*_{8n}$.

Similarly, we substitute steady states into its corresponding Jacobian matrix to evaluate its stability:

$$J_3 = \begin{bmatrix} -\delta_B - \left(\frac{\kappa_A}{1+\gamma_{AB}\cdot B^*}\cdot\left(\frac{A^*}{A_{max}}-1\right) - \left(\frac{A^*\kappa_A}{A_{max}(1+\gamma_{AB}\cdot B^*)}\right)\right) & 0 & \frac{A^*\cdot\gamma_{AB}\cdot\kappa_A}{(1+\gamma_{AB}\cdot B^*+1)^2}\cdot\left(\left(\frac{A^*}{A_{max}}-1\right)\right) \\ -E^*\cdot\left(\frac{\hat{\delta}_{EA}}{(A^*+\hat{A}_{p,th})} - \frac{A^*\cdot\hat{\delta}_{EA}}{(A^*+\hat{A}_{p,th})^2}\right) & -\delta_B - \left(\frac{\kappa_E}{1+\gamma_{EB}\cdot B^*}\cdot\left(\frac{E^*}{E_{max}}-1\right) - \frac{A^*\cdot\hat{\delta}_{EA}}{A^*+\hat{A}_{p,th}} - \left(\frac{E^*\kappa_E}{E_{max}(1+\gamma_{AB}\cdot B^*)}\right)\right) & \frac{E^*\cdot\gamma_{EB}\cdot\kappa_E}{(1+\gamma_{EB}\cdot B^*+1)^2}\cdot\left(\left(\frac{E^*}{E_{max}}-1\right)\right) \\ -B^*\cdot\hat{\delta}_{BA} & 0 & -\kappa_B - A^*\cdot\hat{\delta}_{BA} \end{bmatrix}$$

Steady states when both SA and SE QS-switches are active. When both QS-switches are active, the ODEs cannot be uncoupled to analytically compute the steady states. Therefore, we solve for these steady states numerically by simulating the ODE dynamics starting from an initial condition where $A(t{=}0){=}A_{max}$ and $E(t{=}0){=}E_{max}$ for 10^6 days. If the system converges to a stable state (A^*,E^*,B^*) where both agr switches are active, we double check their stability using the following Jacobian matrix:

$$J_4 = \begin{bmatrix} -\delta_B - \left(\frac{\kappa_A}{1+\gamma_{AB}\cdot B^*}\cdot\left(\frac{A^*}{A_{max}}-1\right) - -\frac{E^*\cdot\hat{\delta}_{AE}}{E^*+\hat{E}_{p,th}} - \left(\frac{A^*\kappa_A}{A_{max}(1+\gamma_{AB}\cdot B^*)}\right)\right) & -A^*\cdot\left(\frac{\hat{\delta}_{AE}}{(E^*+\hat{E}_{p,th})} - \frac{E^*\cdot\hat{\delta}_{AE}}{(E^*+\hat{E}_{p,th})^2}\right) & \frac{A^*\cdot\gamma_{AB}\cdot\kappa_A}{(1+\gamma_{AB}\cdot B^*+1)^2}\cdot\left(\left(\frac{A^*}{A_{max}}-1\right)\right) \\ -E^*\cdot\left(\frac{\hat{\delta}_{EA}}{(A^*+\hat{A}_{p,th})} - \frac{A^*\cdot\hat{\delta}_{EA}}{(A^*+\hat{A}_{p,th})^2}\right) & -\delta_B - \left(\frac{\kappa_E}{1+\gamma_{EB}\cdot B^*}\cdot\left(\frac{E^*}{E_{max}}-1\right) - \frac{A^*\cdot\hat{\delta}_{EA}}{A^*+\hat{A}_{p,th}} - \left(\frac{E^*\kappa_E}{E_{max}(1+\gamma_{AB}\cdot B^*)}\right)\right) & \frac{E^*\cdot\gamma_{EB}\cdot\kappa_A}{(1+\gamma_{EB}\cdot B^*+1)^2}\cdot\left(\left(\frac{E^*}{E_{max}}-1\right)\right) \\ -B^*\cdot\hat{\delta}_{BA} & -B^*\cdot\hat{\delta}_{BE} & -\kappa_B - A^*\cdot\hat{\delta}_{BA} - E^*\cdot\hat{\delta}_{BE} \end{bmatrix}$$

SUPPLEMENTARY REFERENCES

Byrd AL, Deming C, Cassidy SKB, Harrison OJ, Ng WI, Conlan S, et al. Staphylococcus aureus and staphylococcus epidermidis strain diversity underlying pediatric atopic dermatitis. Sci Transl Med 2017;9:eaal4651.

Cau L, Williams MR, Butcher AM, Nakatsuji T, Kavanaugh JS, Cheng JY, et al. Staphylococcus epidermidis protease EcpA can be a deleterious component of the skin microbiome in atopic dermatitis. J Allergy Clin Immunol 2021;147:955–66.e16.

Cheung GYC, Joo HS, Chatterjee SS, Otto M. Phenol-soluble modulins - critical determinants of staphylococcal virulence. FEMS Microbiol Rev 2014;38:698–719.

Clausen ML, Slotved HC, Krogfelt KA, Agner T. Measurements of AMPs in stratum corneum of atopic dermatitis and healthy skin-tape stripping technique. Sci Rep 2018;8:1666.

Cogen AL, Yamasaki K, Sanchez KM, Dorschner RA, Lai Y, MacLeod DT, et al. Selective antimicrobial action is provided by phenol-soluble modulins derived from staphylococcus epidermidis, a normal resident of the skin. J Invest Dermatol 2010;130:192–200.

Daly KM, Upton M, Sandiford SK, Draper LA, Wescombe PA, Jack RW, et al. Production of the Bsa lantibiotic by community-acquired Staphylococcus aureus strains. J Bacteriol 2010;192:1131–42.

dos Santos Nascimento J, Fagundes PC, de Paiva Brito MA, dos Santos KR, do Carmo de Freire Bastos M. Production of bacteriocins by coagulase-negative staphylococci involved in bovine mastitis. Vet Microbiol 2005;106:61–71.

Ebner P, Reichert S, Luqman A, Krismer B, Popella P, Götz F. Lantibiotic production is a burden for the producing staphylococci. Sci Rep 2018;8:7471.

Elias PM. The skin barrier as an innate immune element. Semin Immunopathol 2007;29:3–14.

Fournière M, Latire T, Souak D, Feuilloley MGJ, Bedoux G. Staphylococcus epidermidis and Cutibacterium acnes: two major sentinels of skin microbiota and the influence of cosmetics. Microorganisms 2020;8:1–31.

Geoghegan JA, Irvine AD, Foster TJ. Staphylococcus aureus and atopic dermatitis: a complex and evolving relationship. Trends Microbiol 2018;26:484–97.

Granato ET, Meiller-Legrand TA, Foster KR. The evolution and ecology of bacterial warfare. Curr Biol 2019;29:R521–37.

Harder J, Dressel S, Wittersheim M, Cordes J, Meyer-Hoffert U, Mrowietz U, et al. Enhanced expression and secretion of antimicrobial peptides in atopic dermatitis and after superficial skin injury. J Invest Dermatol 2010;130:1355–64.

Hinds AE, Peterson GX. Method for standardizing staphylococcal suspensions: relationship of optical density to viable cell count. J Bacteriol 1963;86:168.

Hoffman DR, Kroll LM, Basehoar A, Reece B, Cunningham CT, Koenig DW. Immediate and extended effects of sodium lauryl sulphate exposure on stratum corneum natural moisturizing factor. Int J Cosmet Sci 2014;36:93–101.

Hülpüsch C, Tremmel K, Hammel G, Bhattacharyya M, de Tomassi A, Nussbaumer T, et al. Skin pH–dependent Staphylococcus aureus abundance as predictor for increasing atopic dermatitis severity. Allergy 2020;75:2888–98.

Iyer V, Raut J, Dasgupta A. Impact of pH on growth of staphylococcus epidermidis and staphylococcus aureus in vitro. J Med Microbiol 2021:70.

Jabbari S, King JR, Koerber AJ, Williams P. Mathematical modelling of the agr operon in Staphylococcus aureus. J Math Biol 2010;61:17–54.

James EH, Edwards AM, Wigneshweraraj S. Transcriptional downregulation of agr expression in Staphylococcus aureus during growth in human serum can be overcome by constitutively active mutant forms of the sensor kinase AgrC. FEMS Microbiol Lett 2013;349:153–62.

Jenul C, Horswill AR. Regulation of Staphylococcus aureus virulence. Microbiol Spectr 2019;7:3–31.

Junio HA, Todd DA, Ettefagh KA, Ehrmann BM, Kavanaugh JS, Horswill AR, et al. Quantitative analysis of autoinducing peptide I (AIP-I) from Staphylococcus aureus cultures using ultrahigh performance liquid chromatography-high resolving power mass spectrometry. J Chromatogr B Analyt Technol Biomed Life Sci 2013;930:7–12.

Koster MI. Making an epidermis. Ann N Y Acad Sci 2009;1170:7–10.

Le KY, Otto M. Quorum-sensing regulation in staphylococci-an overview. Front Microbiol 2015;6:1174.

Lee NR, Lee HJ, Yoon NY, Kim D, Jung M, Choi EH. Application of topical acids improves atopic dermatitis in murine model by enhancement of skin barrier functions regardless of the origin of acids. Ann Dermatol 2016;28:690–6.

Mathur D, Prakash S, Anand P, Kaur H, Agrawal P, Mehta A, et al. PEPlife: a repository of the half-life of peptides. Sci Rep 2016;6:36617.

Mayville P, Ji G, Beavis R, Yang H, Goger M, Novick RP, et al. Structure-activity analysis of synthetic autoinducing thiolactone peptides from Staphylococcus aureus responsible for virulence. Proc Natl Acad Sci USA 1999;96:1218–23.

Miajlovic H, Fallon PG, Irvine AD, Foster TJ. Effect of filaggrin breakdown products on growth of and protein expression by Staphylococcus aureus. J Allergy Clin Immunol 2010;126:1184–90.e3.

Nakamura Y, Oscherwitz J, Cease KB, Chan SM, Muñoz-Planillo R, Hasegawa M, et al. Staphylococcus δ-toxin induces allergic skin disease by activating mast cells. Nature 2013;503:397–401.

Nakatsuji T, Chen TH, Narala S, Chun KA, Two AM, Yun T, et al. Antimicrobials from human skin commensal bacteria protect against Staphylococcus aureus and are deficient in atopic dermatitis. Sci Transl Med 2017;9:eaah4680.

Olson ME, Todd DA, Schaeffer CR, Paharik AE, Van Dyke MJ, Büttner H, et al. Staphylococcus epidermidis agr quorum-sensing system: signal identification, cross talk, and importance in colonization. J Bacteriol 2014;196:3482–93.

Ong PY, Ohtake T, Brandt C, Strickland I, Boguniewicz M, Ganz T, et al. Endogenous antimicrobial peptides and skin infections in atopic dermatitis. N Engl J Med 2002;347:1151–60.

Otto M, Echner H, Voelter W, Götz F. Pheromone cross-inhibition between Staphylococcus aureus and Staphylococcus epidermidis. Infect Immun 2001;69:1957–60.

Rohatgi A. WebPlotDigitizer. Version 4.6. https://automeris.io/WebPlotDigitizer; 2022. (accessed December 16, 2023).

Timm CM, Loomis K, Stone W, Mehoke T, Brensinger B, Pellicore M, et al. Isolation and characterization of diverse microbial representatives from the human skin microbiome. Microbiome 2020;8:58.

Toribio A, Martínez-Blanco H, Rodríguez-Aparicio L, Ferrero MÁ, Marrodán T, Fernández-Natal I. In vitro adherence of conjunctival bacteria to different oculoplastic materials. Int J Ophthalmol 2018;11:1895–901.

Wei J, Cao X, Qian J, Liu Z, Wang X, Su Q, et al. Evaluation of antimicrobial peptide LL-37 for treatment of Staphylococcus aureus biofilm on titanium plate. Medicine (Baltimore) 2021;100:e27426.

Williams MR, Costa SK, Zaramela LS, Khalil S, Todd DA, Winter HL, et al. Quorum sensing between bacterial species on the skin protects against epidermal injury in atopic dermatitis. Sci Transl Med 2019;11:eaat8329.

Williams MR, Nakatsuji T, Gallo RL. Staphylococcus aureus: Master Manipulator of the Skin. Cell Host Microbe 2017a;22:579–81.

Williams MR, Nakatsuji T, Sanford JA, Vrbanac AF, Gallo RL. Staphylococcus aureus induces increased serine protease activity in keratinocytes. J Invest Dermatol 2017b;137:377–84.

Yap PY, Trau D. Direct E.coli cell count at Od600. https://tipbiosystems.com/wp-content/uploads/2020/05/AN102-E.coli-Cell-Count_2019_04_25.pdf; 2019. (accessed June 7, 2023).

Zhang QY, Bin YZ, Meng YM, Hong XY, Shao G, Ma JJ, et al. Antimicrobial peptides: mechanism of action, activity and clinical potential. Mil Med Res 2021;8:48.

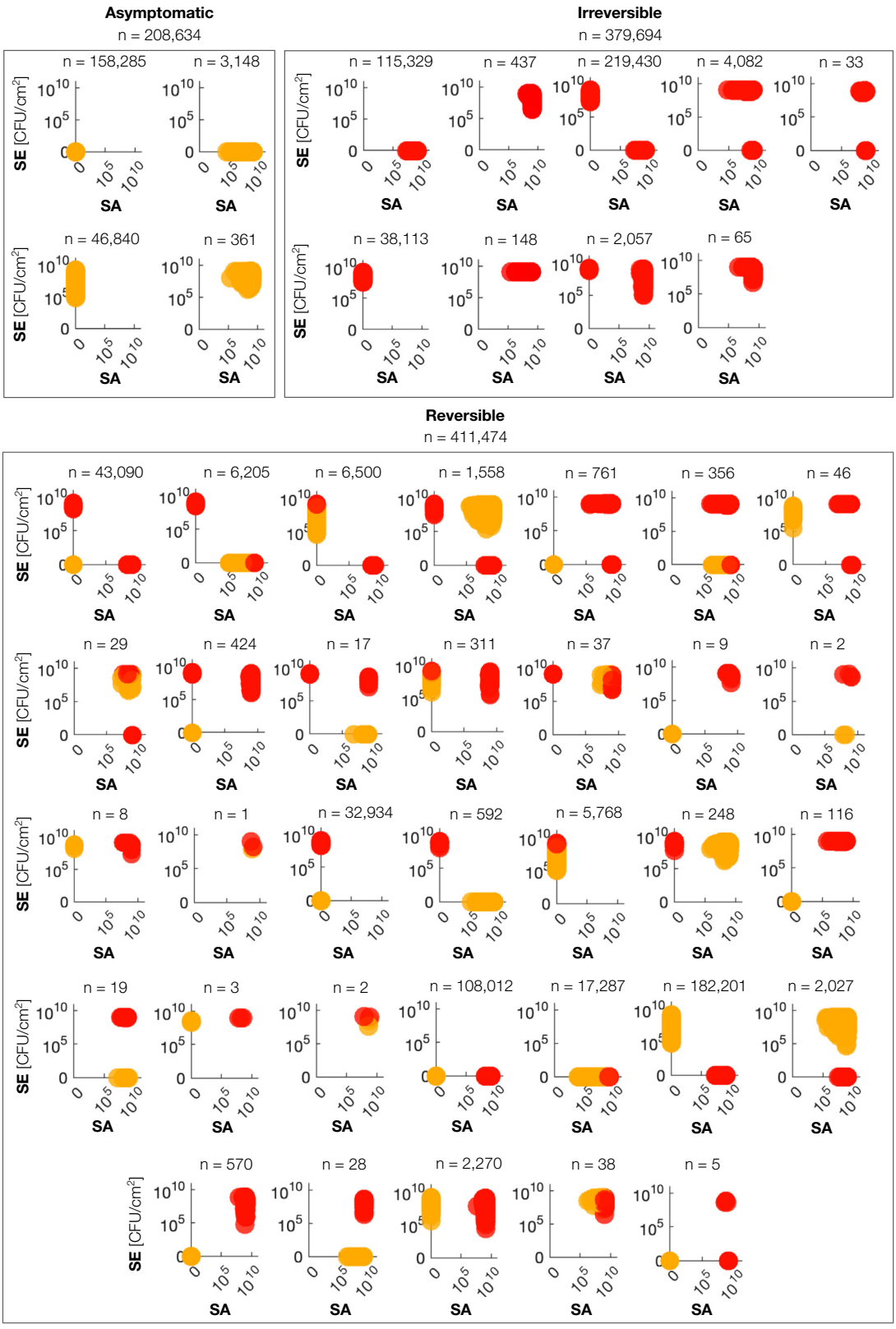

Supplementary Figure S1. Subtypes of virtual AD lesions with SA–SE colonization. All virtual skin sites (10^6 sampled parameter sets) were grouped into subtypes within each of the 3 types on the basis of the number of stable states and composition of SA–SE. The number of virtual skin sites within each subtype is represented by n. Damaged and non-damaged skin states are represented by red and yellow, respectively. AD, atopic dermatitis; SA, *Staphylococcus aureus*; SE, *Staphylococcus epidermidis*.

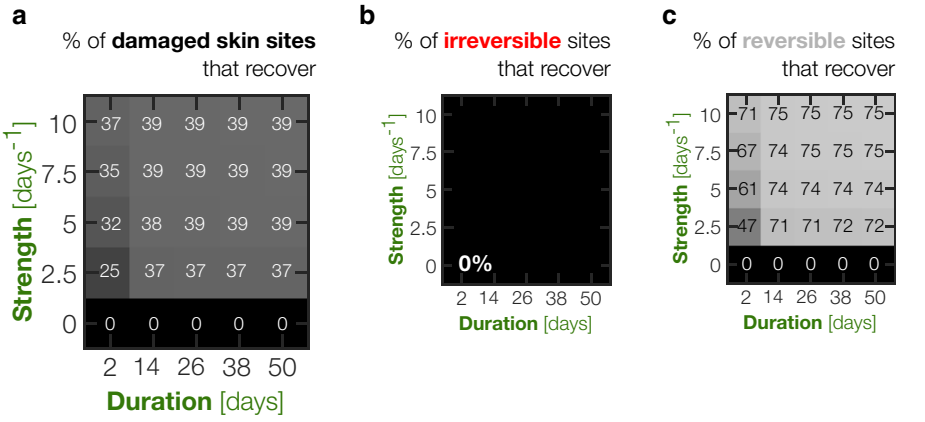

Supplementary Figure S2. Success rate of SA-killing for longer and stronger treatments. (**a**–**c**) The percentage of damaged skin sites that recovered to a non-damaged skin state for (**a**) different treatment strengths and durations and its breakdown for (**b**) irreversible and (**c**) reversible skin sites. SA, *Staphylococcus aureus*.

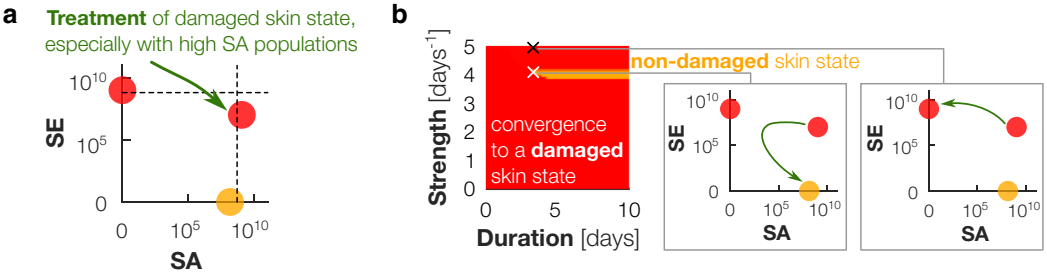

Supplementary Figure S3. SA-killing applied to reversible skin sites can succeed but requires a specific treatment dose and duration. (**a**) SA-killing treatment is applied to damaged skin states with high SA populations. (**b**) Response to SA-killing treatment of varying strengths and durations for an example reversible site, where red represents convergence to a damaged skin state, and yellow represents convergence to a non-damaged skin state. Insets illustrate how treatment strength influences whether convergence to a non-damaged skin state (strength of 4 days^{-1} and duration of 4 days) or damaged skin state (strength of 5 days^{-1} and duration of 4 days) is observed in the model. SA, *Staphylococcus aureus*.

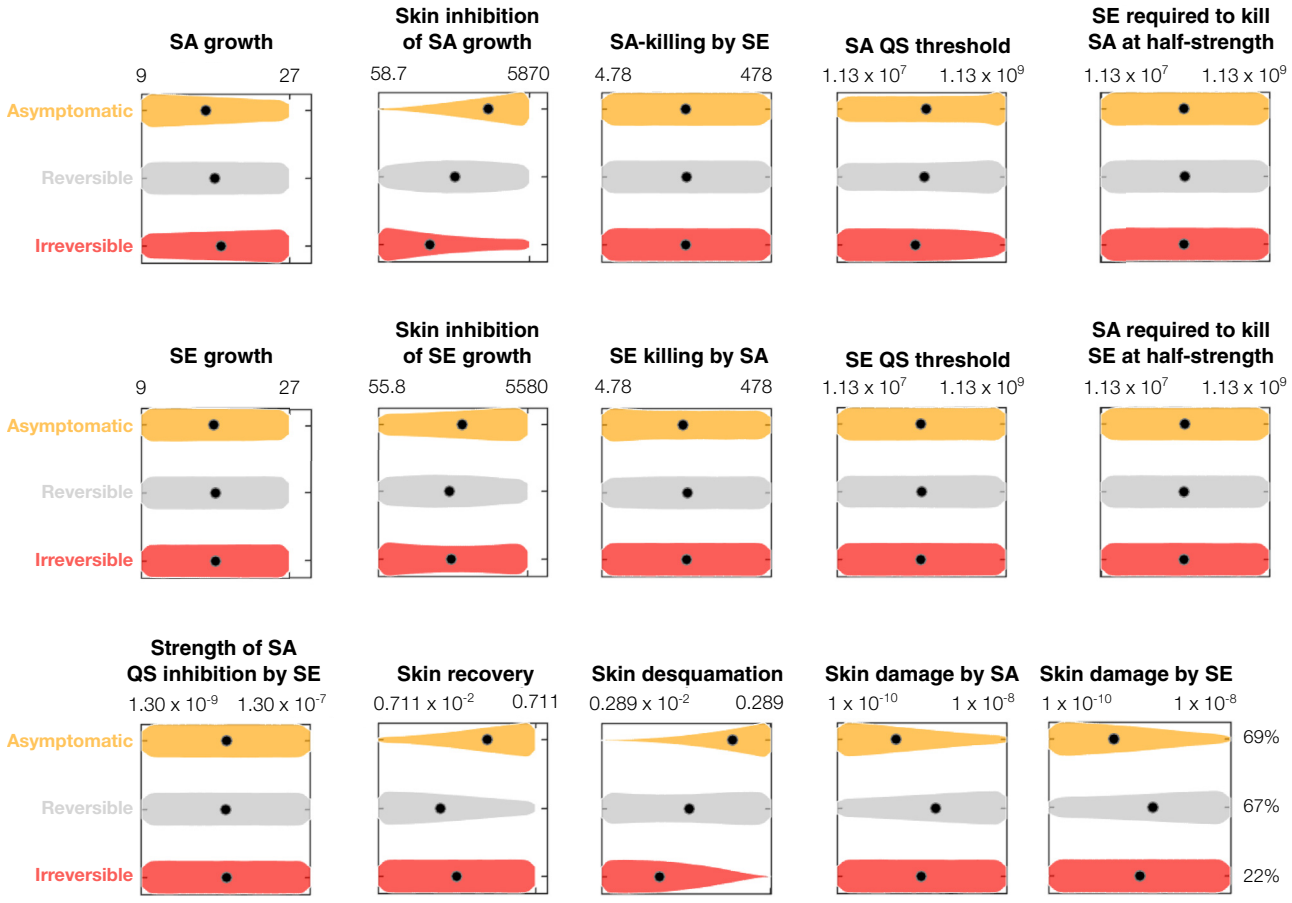

Supplementary Figure S4. Identifying the parameters driving asymptomatic, reversible, and irreversible skin sites. Violin plots of the parameter values making up asymptomatic, reversible, and irreversible sites. Medians are represented by the black dot. Two parameters, the maximum capacities of SA (A_{max}) and SE (E_{max}), were fixed in this study. The skin damage by SE plot (bottom right) does not contain the virtual skin sites (69% of asymptomatic, 67% of reversible, and 22% of irreversible) without skin damage by SE ($\widehat{\delta}_{BE} = 0$). SA, *Staphylococcus aureus*; SE, *Staphylococcus epidermidis*.

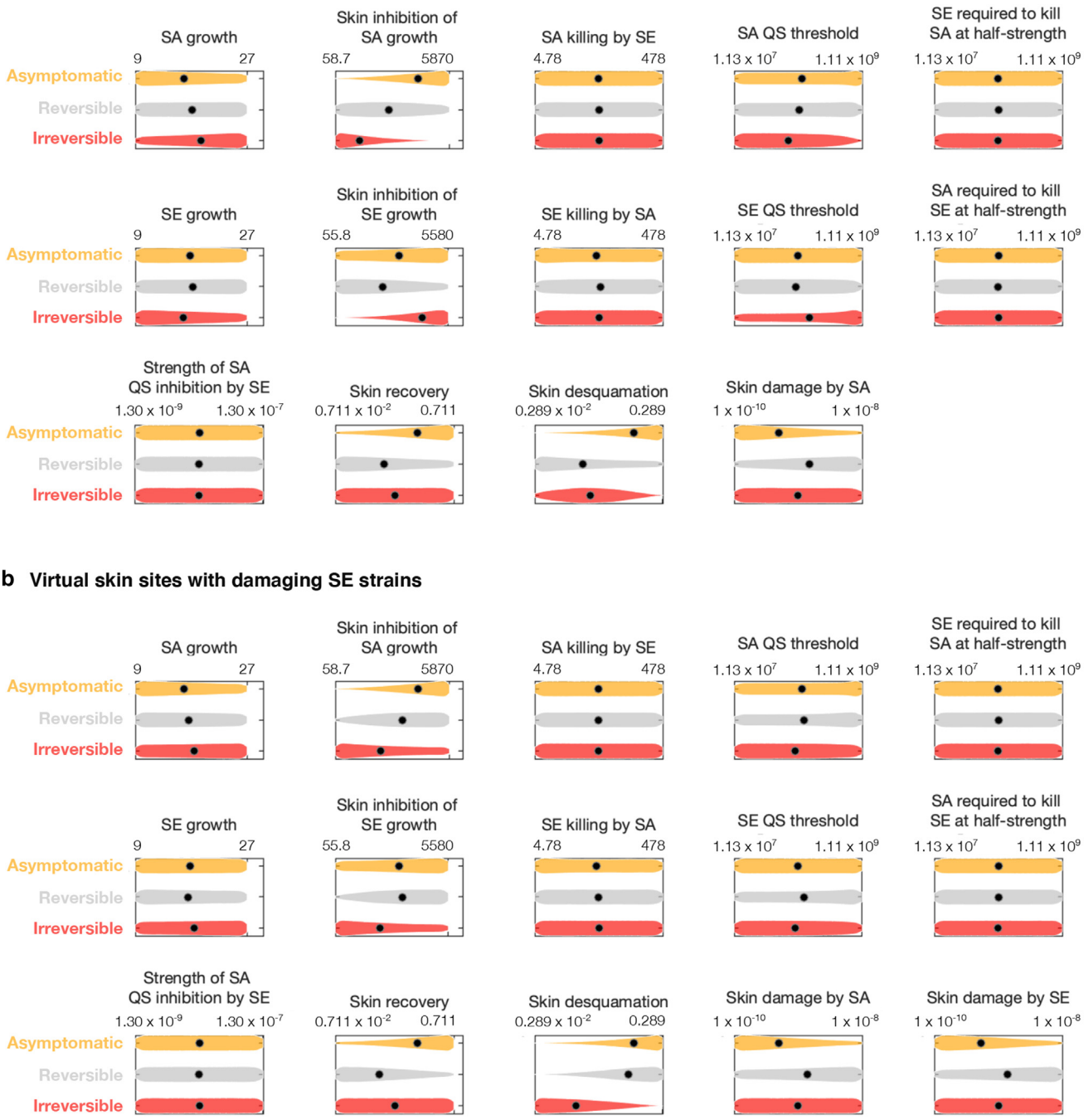

Supplementary Figure S5. Identifying the parameters driving asymptomatic, reversible, and irreversible skin sites for non-damaging and damaging SE strains. **(a)** Non-damaging and **(b)** damaging. Violin plots of the parameter values making up asymptomatic (n = 143,867 for non-damaging SE strains and n = 64,767 for damaging SE strains), reversible (n = 274,263 for non-damaging and n = 137,211 for damaging), and irreversible (n = 82,543 for non-damaging and n = 297,151 for damaging) skin sites. Medians are represented by the black dot. Two parameters, the maximum capacities of SA (A_{max}) and SE (E_{max}), were fixed in this study. SA, *Staphylococcus aureus*; SE, *Staphylococcus epidermidis*.

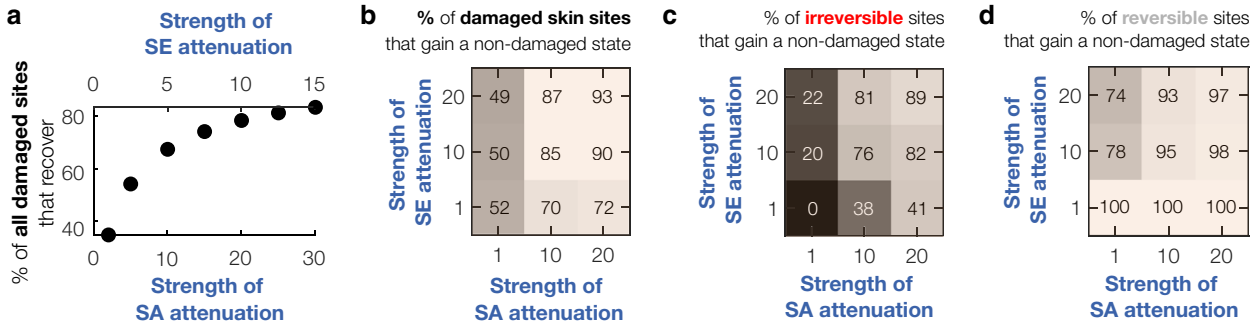

Supplementary Figure S6. Effects of varying levels of SA and SE growth attenuation on dual-action treatment success. (**a**) Percentage recovery of damaged skin sites when a fixed duration (2 days) and strength (3 $days^{-1}$) of SA-killing is applied, and SA and SE growth attenuations are varied. The respective attenuation of SA and SE growths by treatment, γ_{AS} and γ_{ES}, were fixed at a γ_{AS}: γ_{ES} ratio of 2:1 on the basis of data from Iyer et al (2021), which indicated that SA growth is attenuated approximately twice as much as SE growth for decreasing levels of pH from pH 7 to pH 5, a range we would expect if applying a hydrochloric acid cream of pH 3.5 to attenuate SA and SE growths (Lee et al, 2016). (**b**–**d**) Percentage of (**b**) damaged, (**c**) irreversible, and (**d**) reversible skin sites that gain a non-damaged skin state when SA and SE growth attenuation is enhanced by different strengths. SA, *Staphylococcus aureus*; *Staphylococcus epidermidis*.

Supplementary Figure S7. Mathematical model schematic of AD lesional skin with SA–SE colonization. Each interaction is labeled with the corresponding parameter in the model equations. AD, atopic dermatitis; SA, *Staphylococcus aureus*; SE, *Staphylococcus epidermidis*.

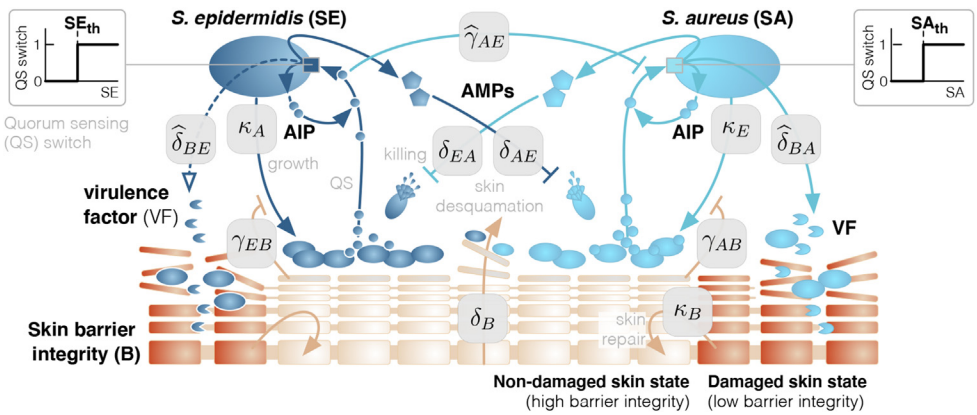

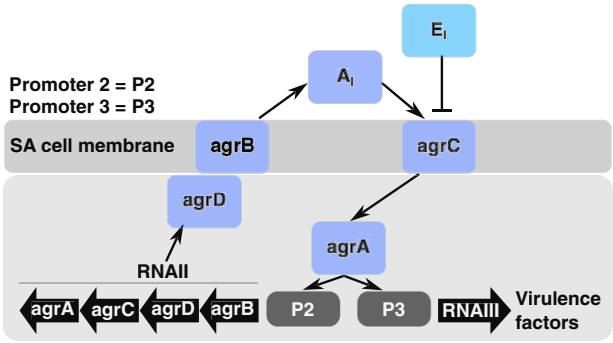

Supplementary Figure S8. Illustration of the agr system in *Staphylococci*. This was adapted from the studies by Le and Otto (2015) and Jabbari et al (2010). RNAII encodes 4 genes: agrB, agrD, agrC, and agrA, each with a different function: agrB and agrD synthesize and control the secretion of signaling molecule AIP, and agrC and agrA make up a 2-component signal receptor that increases the expression of RNAII and RNAIII. RNAIII controls the expression of *Staphylococci* virulence factors, where those of SA can activate damaging of the skin barrier integrity (Williams et al, 2017a). agr, accessory gene regulator; AIP, autoinducing peptide; SA, *Staphylococcus aureus*.

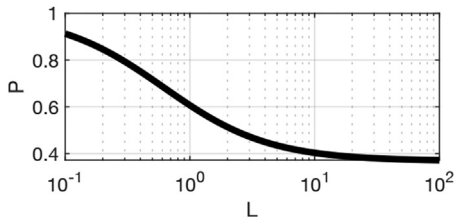

Supplementary Figure S9. Plot of the function $P(t) = P_0 \cdot e^{-\delta \cdot \frac{L}{L+L_{th}} \cdot t}$, which models the killing of a bacterial population for (logarithmic) titrations of an antimicrobial agent. The function displays the typical sigmoidal shaped dose–response as observed in experimental data in the literature.

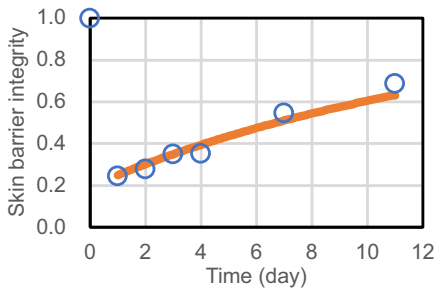

Supplementary Figure S10. Fitting the model to data from Hoffman et al (2014) to estimate skin barrier repair rate. Data describes the TEWL measured from healthy individuals (n = 20) after they wore a patch of sodium lauryl sulphate for 24 hours in the forearm. Data points were converted into 1/TEWL (open circles). Fitted model of the skin barrier recovery in Equation S30 is shown by the solid line. TEWL, transepidermal water loss.

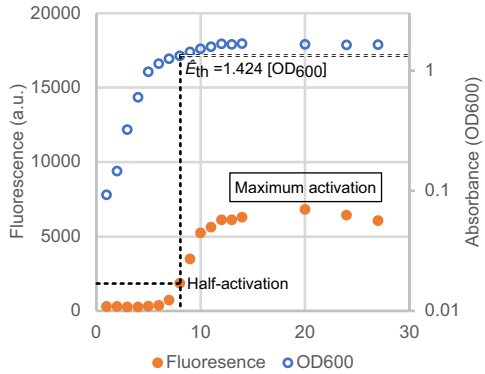

Supplementary Figure S11. Data extracted from Olson et al (2014) were used to estimate the population density threshold activating SE agr switch ($\hat{E}_{th}$). We identified the time at which half of the maximum agr expression is achieved (black dashed lines), as measured by the expression of fluorophores encoded downstream of the agr promoter (orange filled circles, left y-axis), and extracted the population density of SE WT 1457 grown in TSB (measured by optical density, blue open circles, right y-axis) at that time ($\hat{E}_{th}$). agr, accessory gene regulator; SE, *Staphylococcus epidermidis*; TSB, tryptic soy broth.

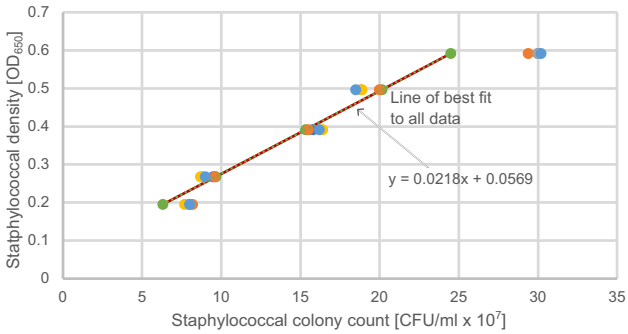

Supplementary Figure S12. Linear fit to data from Hinds and Peterson (1963) **relating staphylococcal density [OD_{650}] and staphylococcal colony counts [CFU/ml×10^7].** Circles show the data points taken from Hinds and Peterson (1963), and red line shows the fitting. CFU, colony-forming unit; OD, optical density.

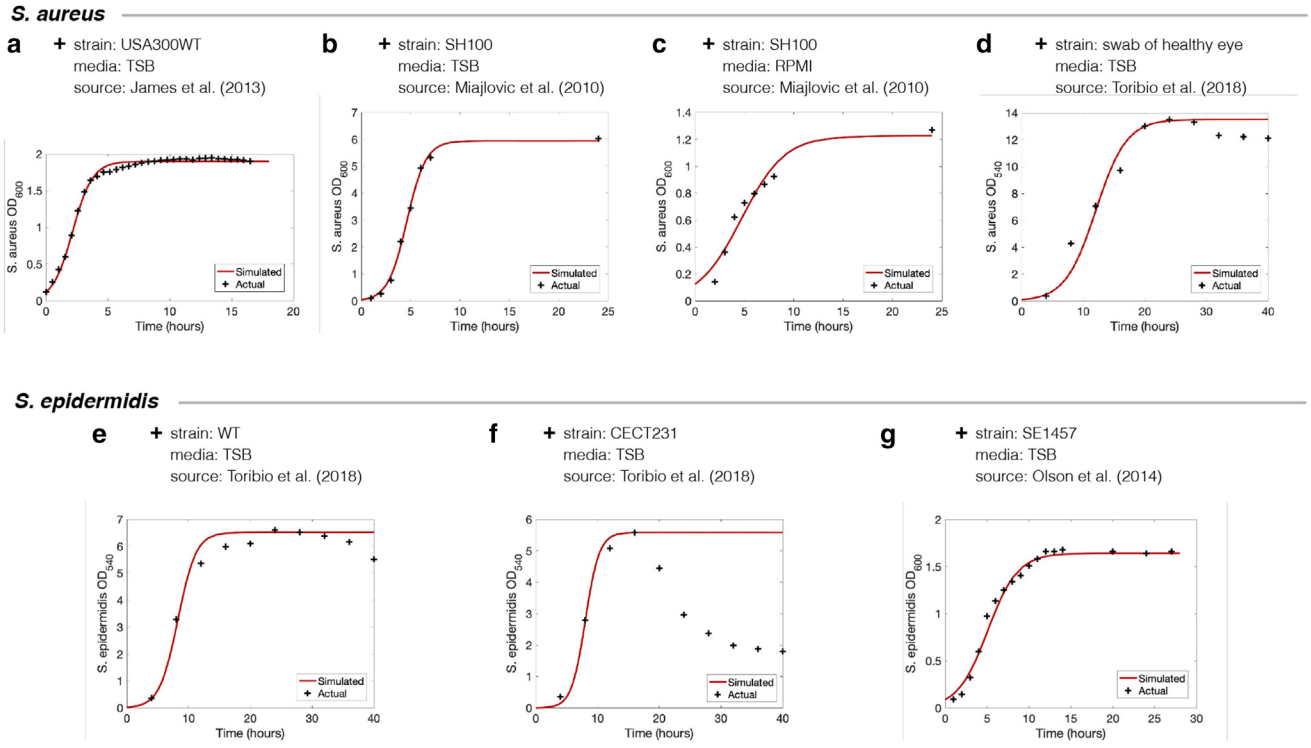

Supplementary Figure S13. Fits of model to experimental data to estimate growth rates and carrying capacities. Least-square fits of the model of logistic growth of SA and SE from Equations S33 and S34 (red curves) to numerous time-course growth data from the literature (black crosses). The strain of (**a**–**d**) SA and (**e**–**g**) SE, the media in which they were grown, and the published paper from which the data were extracted are detailed above the respective plot. SA, *Staphylococcus aureus*; SE, *Staphylococcus epidermidis*.

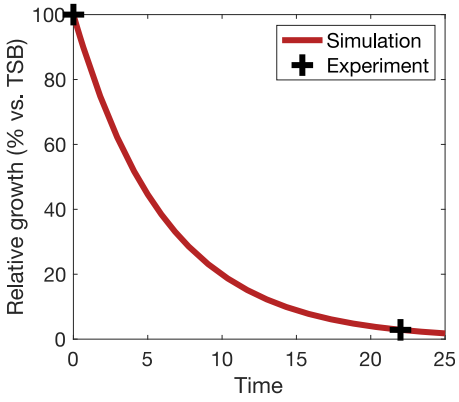

Supplementary Figure S14. Simulated curve of SA death (solid curve) by fitting to Equation S36 **to the extracted data from** Nakatsuji et al (2017) **(crosses).** Extracted data measured the relative growth of SA in spent supernatant of SE AMT1-A9 grown to a maximum density in overnight cultures at 37 °C (crosses). The impact on SA growth by supernatant media of 100 μl of SE AMT1-A9 was evaluated by adding 1×10^4 CFU of SA and aerobically culturing at 37 °C for 22 hours. CFU, colony-forming unit; SA, *Staphylococcus aureus*; SE, *Staphylococcus epidermidis*.

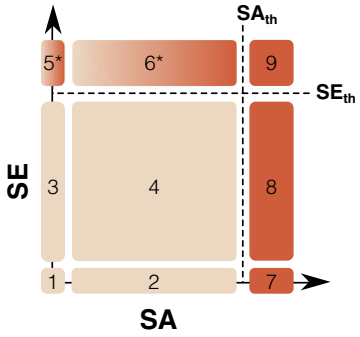

Supplementary Figure S15. Schematic of the 9 possible characteristic population densities of SA and SE leading to a non-damaged or damaged skin state in the model. SA_{th} and SE_{th} represent the respective SA and SE population thresholds for QS-switches to activate. Regions lying on the axes (1, 2, 3, 4, 5, and 7) have 1 collapsed population (ie, SA or SE are at zero populations). Regions 1−4 converge to a non-damaged skin state (colored beige). Regions 7−9 converge to a damaged skin state (colored red). *For regions where only SE QS-switch is active (5 and 6), the skin state may be non-damaged or damaged depending on whether the SE strain for a particular virtual skin site is skin damaging ($\hat{\delta}_{BE} > 0$) or not ($\hat{\delta}_{BE} = 0$). QS, quorum sensing; SA, *Staphylococcus aureus*; SE, *Staphylococcus epidermidis*.

Supplementary Table S1. Table of all Model Parameters

Parameters	Description	Nominal Values	Range Explored	Units	Source
Parameters of the dynamics associated with SA					
κ_A	Maximum growth rate of SA	17.9	[9, 27]	1/day	James et al, 2013; Miajlovic et al, 2010; Olson et al, 2014; Toribio et al, 2018
A_{max}	Carrying capacity of SA population	11.1	—	10^8 CFU/cm^2	James et al, 2013; Miajlovic et al, 2010; Olson et al, 2014; Toribio et al, 2018
γ_{AB}	Effective strength of inhibition on SA growth by a high skin barrier integrity	587	587× [10^{-1}, 10]	n/a	—
δ_{AE}	Death rate of SA from killing by SE AMP	478	478×[10^{-2},1]	1/day	Nakatsuji et al, 2017
$\widehat{A}_{th}$	Threshold population of SA that activates the QS-switch	1.13	[1.13×10^{-1}, A_{max}]	10^8 CFU/cm^2	Olson et al, 2014
$\widehat{E}_{p,th}$	Population of SE required to kill SA at half-strength	1.13	[1.13×10^{-1}, A_{max}]	10^8 CFU/cm^2	—
$\widehat{\gamma}_{AE}$	Strength at which SE inhibits SA QS-switch on	1.30	1.30 × [10^{-1}, 10]	1/(10^8 CFU/cm^2)	Williams et al, 2019
Parameters of the dynamics associated with SE					
κ_E	Maximum growth rate of SE	17.0	[9, 27]	1/day	Olson et al, 2014; Toribio et al, 2018
E_{max}	Carrying capacity of SE population	11.1	—	10^8 CFU/cm^2	Olson et al, 2014; Toribio et al, 2018
γ_{EB}	Effective strength of inhibition on SE growth by a high skin barrier integrity	558	558 × [10^{-1}, 10]	n/a	—
δ_{EA}	Death rate of SE from killing by SA AMP	478	478×[10^{-2},1]	1/day	Nakatsuji et al, 2017
$\widehat{E}_{th}$	Threshold population of SE that activates the QS-switch	1.13	[1.13×10^{-1}, E_{max}]	10^8 CFU/cm^2	Olson et al, 2014
$\widehat{A}_{p,th}$	Population of SA required to kill SE at half-strength	1.13	[1.13×10^{-1}, A_{max}]	10^8 CFU/cm^2	—
Parameters of the dynamics modelling the state of the skin barrier integrity					
κ_B	Rate of skin turnover	0.0711	0.0711× [10^{-1}, 10]	1/day	Hoffman et al, 2014
δ_B	Rate of skin shedding	0.0289	0.0289× [10^{-1}, 10]	1/day	Koster, 2009
$\widehat{\delta}_{BA}$	Rate of damage of skin barrier integrity by virulence factors of SA	0.1	0.1×[10^{-1}, 10]	cm^2/(10^8CFU · day)	—
$\widehat{\delta}_{BE}$	Rate of damage of skin barrier integrity by virulence factors of SE	0.1	0.1×[10^{-3}, 10][1]	cm^2/(10^8CFU · day)	—

Abbreviations: AMP, antimicrobial peptide; CFU, colony-forming unit; max, maximum; QS, quorum sensing; SA, *Staphylococcus aureus*; SE, *Staphylococcus epidermidis*.

[1]When sampled values of $\widehat{\delta}_{BE} < 1 \times 10^{-2}$ cm^2/(10^8CFU day), we set $\widehat{\delta}_{BE} = 0$ to account for some SE strains being non-skin damaging.

Supplementary Table S2. Summary of Estimated (κ_A,A_{max}) and (κ_E,E_{max}) Values from 4 Data Sources

Reference Data Source	Fitting in Supplementary Figure S13	Estimated (κ_A[day^{-1}], A_{max}[OD])	Estimated (κ_E[day^{-1}], E_{max}[OD])
James et al, 2013	(a)	(26.2, 1.91)	
Miajlovic et al, 2010	(b)	(23.3, 6.03)	
	(c)	(12.4, 1.20)	
Toribio et al, 2018	(d)	(9.75, 13.5)	
	(e)		(16.2, 6.52)
	(f)		(21.4, 5.58)
Olson et al, 2014	(g)		(13.5, 1.64)

Abbreviations: max, maximum; OD, optical density.

The fitting of the model in Equations S33 and S34 are shown in Supplementary Figure S13.

Supplementary Table S3. SA agr (I) Activity in the Presence and Absence of SE AIPs (Data Extracted from Williams et al [2019])

Media Condition	SA agr (I) Activity (% Relative Fluorescence Units to Control)
Control	100
Supernatant of SE WT	11.0
Supernatant of SE Δ AIP	128

Abbreviations: agr, accessory gene regulator; AIP, autoinducing peptide; SA, *Staphylococcus aureus*; SE, Staphylococcus epidermidis; WT, wild type.

We use the measurement of SA agr (I) activity grown in cell-free spent media of SE WT as the measurement for A_{agr_epi} and its activity when grown in cell-free spent media of SE Δ AIP as the measurement for $A_{agr\_no\_epi}$.